nature communications

Article

https://doi.org/10.1038/s41467-025-60516-8

Mechanism of human α3β GlyR regulation by intracellular M3/M4 loop phosphorylation and 2,6-di-tert-butylphenol interaction

Received: 16 May 2024

Accepted: 24 May 2025

Published online: 05 June 2025

Check for updates

Xiaofen Liu, Malgorzata Krezel & Weiwei Wang

α3β glycine receptor (GlyR) is a subtype of GlyRs that belongs to the Cys-loop receptor superfamily. It is highly expressed in the spinal dorsal horn where sensory information is integrated. Under inflammatory conditions, the large unstructured intracellular M3/M4 loops of the α3 subunit are phosphorylated through the prostaglandin E2 (PGE_2) pathway, inhibiting ion conduction, and resulting in elevated pain sensation. A small molecule analgesic analog, 2,6-di-tert-butylphenol (2,6-DTBP) potentiates phosphorylated α3β GlyR through unclear mechanisms and relieves pain. Combining cryo-Electron Microscopy (cryo-EM) structures and single molecule Förster resonance energy transfer (smFRET) experiments, we show compaction of M3/M4 loop towards the ion conduction pore upon phosphorylation and further by 2,6-DTBP binding, which in turn modulates function through changing pore conformations and local electrostatics. We show that simultaneous interactions with the M3/M4 loop and the transmembrane domain (TM) is necessary for the potentiation of heteromeric α3β GlyR by 2,6-DTBP, while TM interaction alone is sufficient to potentiate homomeric α3 GlyR, explaining the mystery of why 2,6-DTBP potentiates only phosphorylated α3β GlyR. These findings show how post-translational modification of the unstructured intracellular M3/M4 loop may regulate Cys-loop receptor function, providing new perspectives in pain control and other pharmaceutical development targeting GlyRs and other Cys-loop receptors.

GlyRs are members of the ionotropic pentameric Cys-loop receptor superfamily and mediate inhibitory neurotransmission in the central nervous system[1,2]. In adult animals, heteromeric GlyRs consisting of both α (α1-α4) and β subunits with a 4α:1β stoichiometry are the dominant form[3–5]. Dysfunction or altered expression/trafficking of GlyRs in the brain is associated with multiple neurological disorders, including Alzheimer's disease[6,7], schizophrenia[8–10], epilepsy[11,12], and autism[8]. In the spinal cord, GlyRs are highly expressed and play major roles in inhibitory neurotransmission, with preferences in localization and physiology depending on subtypes[1,2,13–15]. The α1β/α2β subtypes of GlyRs are found throughout the spinal cord and governs locomotive and sensory function,s and harbor mutagenic sites that cause the congenital disease hyperekplexia[16–20], while the α3β GlyR is found more concentrated in the superficial layers of the dorsal horn, where sensory signals are processed before entering the brain[1,2,21,22].

Chronic pain is a very common problem that affects over 20% individuals in the US and world-wide[23–25]. α3β GlyR is an essential player in inflammation related hyperalgesia (increased perception of pain)[26,27] and a promising drug target for non-psychoactive pain control[27–30]. Unlike most GlyR-related disordered, where loss of function mutations are the major culprit, α3β GlyR modulates pain sensation through post-translational modification in the large internal M3/M4 loop (~80 amino acid residues)[26,31]. This loop is responsible for post-synaptic localization (β subunit) and involved in gating property modulation of

Departments of Biophysics, University of Texas Southwestern Medical Center, Dallas, TX, USA. e-mail: Weiwei.Wang@UTSouthwestern.edu

GlyRs[32–38]. Phosphorylation at S346 of the GlyR α3 subunit has been well characterized for its functional effects and pharmacological relevance[26,39–42]. Prostaglandin E2 (PGE_2) produced under inflammatory conditions activates the Prostaglandin E2 receptor 2 (EP_2), which in turn results in protein kinase A (PKA)-dependent phosphorylation of residue S346 in the large internal M3/M4 loop of the GlyR α3 subunit, reducing Cl^- conduction[26,42,43] (Fig. 1a). Unfortunately, partly due to the lack of structural information, how a phosphorylation in an unstructured loop away from the pore (~50 aa) modulates ion conduction is unclear[38,39,42].

A derivative of the general anesthetic propofol, 2,6-di-*tert*-butylphenol(2,6-DTBP), that does not bind to γ-Aminobutyric Acid type A ($GABA_A$) receptors and is non-psychoactive[44], potentiates α3β GlyR and alleviates hyperalgesia in a mouse model of neuropathic pain[40,45].

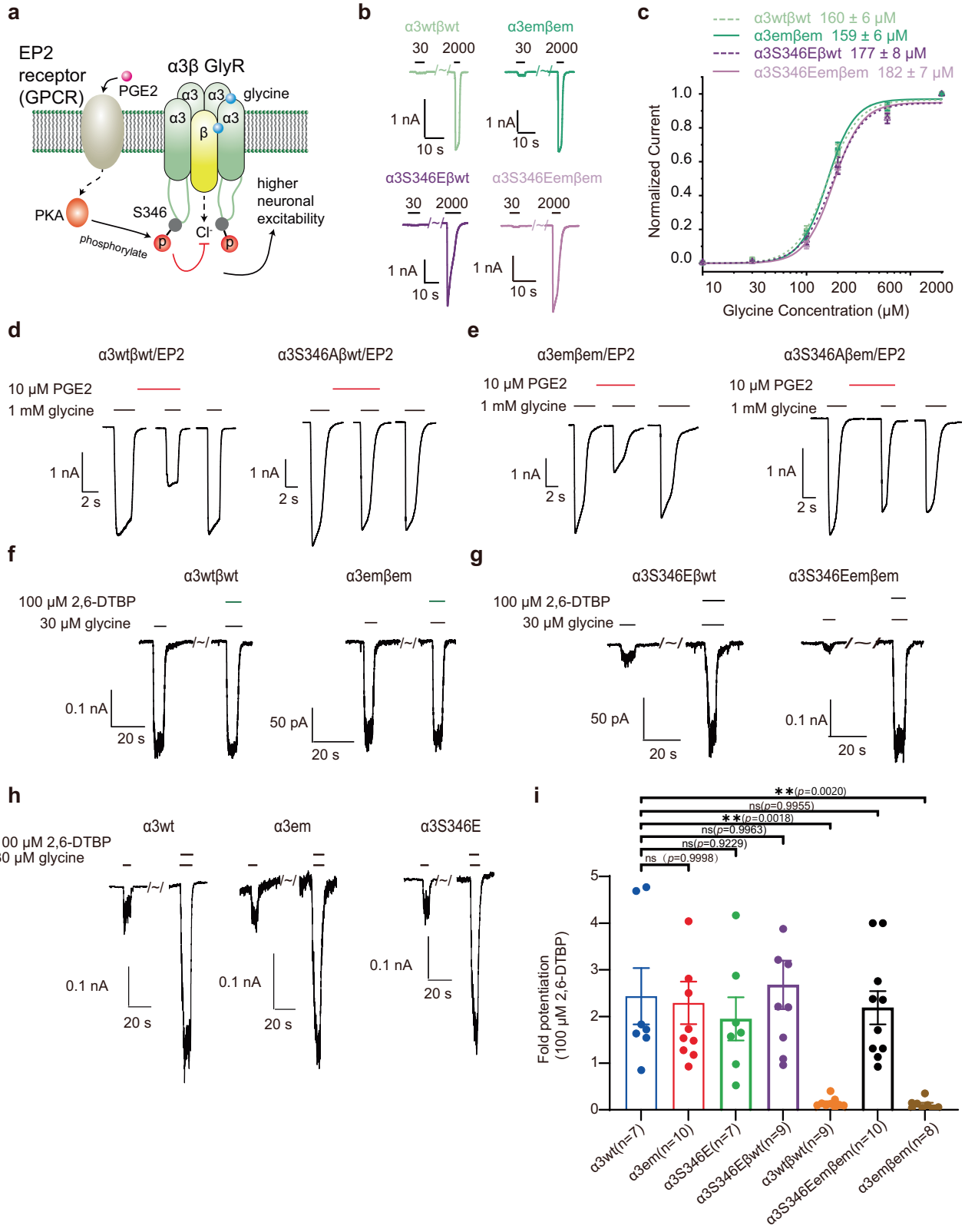

Fig. 1 | Functional characterization of human α3β GlyR. a The effect of PGE_2 on glycinergic signaling. PGE_2 activates EP_2 receptors, which in turn phosphorylate α3 subunits in a PKA-dependent manner and inhibits Cl^- flux through α3β GlyR. **b** Typical glycine response of α3wtβwt, α3emβem, α3S346Eβwt and α3S346Eemβem at 30 μM and 2 mM glycine concentration. **c** Dose response with Hill fits (lines). Data are represented as mean ± S.E.M. (α3wtβwt: $n = 7$ cells, α3emβem: $n = 7$ cells, α3S346Eβwt: $n = 11$ cells, α3S346Eemβem: $n = 7$ cells). **d**, **e** Representative recordings showing the effect of 10 μM PGE_2 on glycine-evoked current in HEK293T cells co-transfected with the EP2 receptor and **d** α3wtβwt, and **e** α3emβem. PKA consensus sequence mutation S346A is present in the right panels. **f**, **g**, **h** Representative whole-cell recordings of glycine-induced currents in the absence and presence of 100 μM 2,6-DTBP in HEK293T cells expressing **f** α3wtβwt (left) and α3emβem (right) GlyRs, **g** α3S346Eβwt (left) and α3S346Eemβem (right), and **h** α3wt (left), α3em (middle), α3S346E (right). **i** Fold-increase in 30 μM glycine-evoked currents of α3wtβwt, α3emβem, α3S346Eβwt, α3S346Eemβem, α3wt, α3em and α3S346E by 100 μM 2,6-DTBP. Data are represented as mean ± S.E.M. *P*-values were calculated using one-way ANOVA. (**$p < 0.01$; ns, not significant. The exact *p*-values are shown in the figure).

The positive modulating effect of 2,6-DTBP appears to be dependent on the phosphorylation of α3β GlyR[40,42], and related to an aromatic amino-acid residue (F388 of human α3 subunit) near the intracellular opening of the conduction pore[46]. Although 2,6-DTBP is currently not suitable for analgesic use in humans due to toxicity concerns, understanding its working mechanism will provide guidance for the design of effective and safe GlyR-targeting pain control agents without psychoactive effects. However, the working mechanism of 2,6-DTBP remains mysterious. The lack of structural information of the α3β GlyR and the unstructured nature of the M3/M4 loop in human GlyRs have severely limited our understanding of α3β GlyR regulation in pain.

In this work, we report 3.8 Å resolution cryo-EM structures of the human heteromeric α3β GlyR bound with glycine (α3β-gly) both in detergent (digitonin) and a membrane mimetic (saposin nanodisc), showing minimal differences between the two. We also determined 3.6–3.7 Å resolution structures of a phosphorylation mimetic form[40,42], (α3S346Eβ-gly), and its complex with 2,6-DTBP (α3S346Eβ-gly/2,6-DTBP), where we observed asymmetrical pore rearrangements upon phosphorylation and 2,6-DTBP binding. Since the M3/M4 loop is missing in these structures due to flexibility, we used the single-molecule Förster resonance energy transfer (smFRET) method to characterize its relative position with respect to the ion conduction pore. We observed compaction of M3/M4 loop upon phosphorylation (S346E), and further compaction towards the pore by 2,6-DTBP binding that correlates with pore conformational changes. Further mutagenesis and electrophysiology demonstrated dual requirement of transmembrane domain (TM) and M3/M4 loop phosphorylation for 2,6-DTBP potentiation of the α3β GlyR, but only the TM is required for homomeric α3 GlyR potentiation. Combining structural, electrophysiological, and smFRET observations, we propose a mechanism where compaction of phosphorylated M3/M4 loop towards the pore regulates function by altering pore conformation and local electrostatics, while 2,6-DTBP potentiates α3β GlyR through simultaneous interactions with the TM and phosphorylated M3/M4 loop. This mechanism helps in understanding the regulation of α3β GlyR in inflammatory pain, and the possible development of new pharmacological agents. In addition, it provides a framework for understanding how unstructured M3/M4 loops regulate Cys-loop receptor function through post-translational modification.

Results

Engineered GlyR recapitulates wild-type modulation in the PGE2 pathway

Wild-type α3wtβwt GlyR aggregated in purification attempts for structural characterization. To mitigate this, we generated α3em through a small deletion in the M3/M4 loop without affecting the PKA consensus phosphorylation sequence (RESR, positions 344-347, Supplementary Fig. 1a). The S346E mutation, a good mimetic of phosphorylation that recapitulates GlyR activity regulation[21,39,42], was also made for both α3em and α3wt.

Co-expression of α3em (this study) and the βem (reported previously, Supplementary Fig. 1b)[3,5,38] led to higher expression levels and a more monodispersed peak on size exclusion chromatography compared to the wild-type (Supplementary Fig. 1c), while retaining indistinguishable glycine EC_{50} (~160 μM) and Hill slope (~3) (Fig. 1b, c, Supplementary Fig. 1f green and light green). S346E had a marginal effect on glycine activation: increasing glycine EC_{50} of both α3emβem and α3wtβwt GlyR to ~180 μM without changing Hill slope (Fig. 1b, c, Supplementary Fig. 1f purple and light purple).

Ion conduction of α3emβem GlyR and α3wtβwt GlyR was similarly modulated through EP_2 receptor activation. Application of 10 μM PGE_2 to HEK293T cells co-expressing EP_2 receptors reduced glycine-evoked currents by ~50% for both α3wtβwt and α3emβem GlyR (Fig. 1d, e left panels). Mutation of the phosphorylation site, S346A, abolished this effect (Fig. 1d, e right panels). Consistent with previous reports[40], 2, 6-DTBP strongly potentiated glycine-induced currents for both α3wtβwt (3.7 ± 0.5 folds, $n = 9$) and α3emβem (3.2 ± 0.4 folds, $n = 10$) GlyR only after phosphorylation (S346E mimetic, Fig. 1f, g, i). At the same time, we also verified that truly phosphorylated α3emβem can also be potentiated by 2,6-DTBP (Supplementary Fig. 1h). On the other hand, 2,6-DTBP potentiated homomeric α3 GlyR both without phosphorylation (α3wt, 3.4 ± 0.6 folds, $n = 7$; α3em 3.3 ± 0.5 folds, $n = 10$) and with phosphorylation (mimic) (α3S346E 2.9 ± 0.6 folds, $n = 7$) (Fig. 1h, i).

Taken together, α3emβem GlyR recapitulates functional properties of wild-type α3β GlyR in glycine-activation, PGE_2-dependent modulation, as well as 2,6-DTBP potentiation.

S346 phosphorylation and 2,6-DTBP binding alter ion-conduction pore conformation

To elucidate how phosphorylation at α3S346 and 2,6-DTBP modulates glycine-elicited α3β GlyR currents, we resolved glycine-bound structures of α3emβem GlyR (α3β-gly, 3.8 Å, Supplementary Fig. 2a–e), phosphorylation mimic α3emS346Eβem GlyR (α3S346Eβ-gly, 3.7 Å, Supplementary Fig. 3a–e), and phosphorylation mimic α3emS346Eβem GlyR with 2,6-DTBP (α3S346Eβ-gly/2,6-DTBP, 3.6 Å, Supplementary Fig. 3f–j), in digitonin detergent. To identify structural changes arising from detergent/lipid mimetic biochemistry, we also resolved glycine-bound structure of α3emβem GlyR reconstituted in saposin nanodiscs (α3β-gly (nanodisc), 3.8 Å, Supplementary Fig. 2f–j). All density maps allowed unambiguous model-building (Supplementary Fig. 2–4) and showed a 4:1 α3:β subunit stoichiometry (Fig. 2a, b), consistent with the stoichiometry in other two major human heteromeric GlyR subtypes, $\alpha1\beta$[5,47] and $\alpha2\beta$[3], as well as a zebrafish analog $\alpha1\beta_B$[48]. The structures in digitonin and nanodiscs were virtually identical throughout the extracellular (ECD) and transmembrane domains (TM) (Fig. 2d, e, Supplementary Fig. 5a–e, Supplementary Fig.6a, c, d), with a RMSD of ~0.9 Å, suggesting that digitonin provides a suitable biochemical environment for characterizing GlyR structures. All structures were determined using α3emβem GlyRs in this work and they are noted as α3β GlyR afterwards for simplicity.

The α3β-gly structures (in both digitonin and nanodiscs) showed a pore conformation typical of a desensitized GlyR channel[3,5,47,49–51] (Fig. 2c, d). The gate at the 9′ position (α3: L261, β: L285) is in the open conformation, while a constriction (~2.1 Å radius) at -2′ was observed (Fig. 2c, d, e). A pseudo-5-fold symmetry was maintained throughout the ECD (Supplementary Fig. 6b, d) and TM.

https://doi.org/10.1038/s41467-025-60516-8

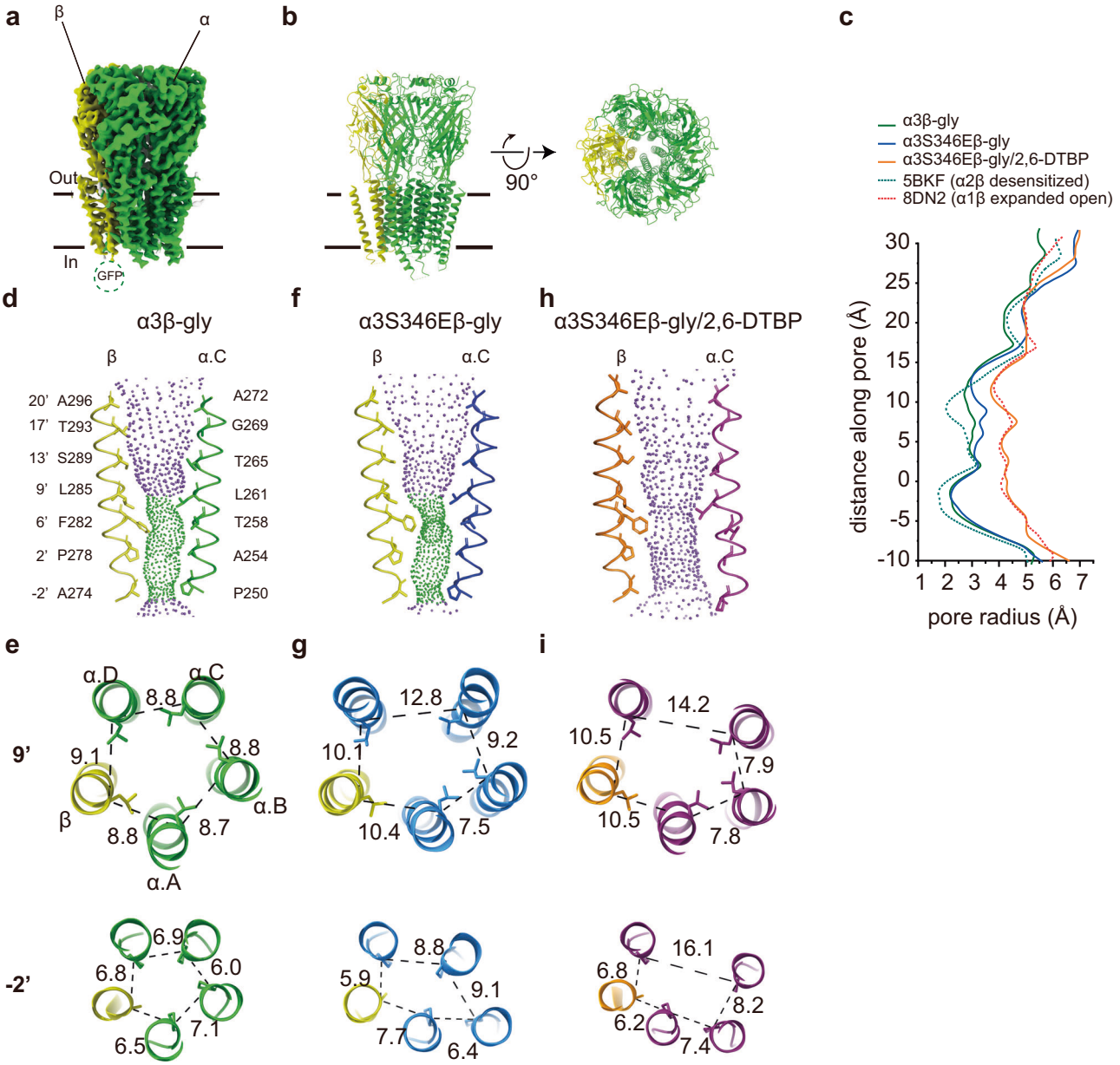

Fig. 2 | Conformational differences between α3β-gly, α3S346Eβ-gly, and α3S346Eβ-gly/2,6-DTBP GlyRs. a Side view of the cryo-EM map of α3β GlyR in digitonin in the presence of glycine. **b** Side (left) and top-down (right) view of the atomic models. α3 subunits and β subunit are respectively colored in bright green and yellow. **c** Plot of pore radii calculated by the HOLE program for the α3β-gly (green), α3S346Eβ-gly (blue), α3S346Eβ-gly/2,6-DTBP (orange), α2β-gly (desensitized, PDB ID: 5BKF, green dashed line), and α1β-gly (expanded open, PDB ID:8DN2, red dashed line). **d**, **f**, **h** Ion permeation pathways for **d** α3β-gly, **f** α3S346Eβ-gly, and **h** α3S346Eβ-gly/2,6-DTBP GlyRs. M2 helices are shown as cartoons, and the side chains of pore-lining residues as sticks. Purple, green, and red spheres define radii of > 3.3 Å, 1.8-3.3 Å, and <1.8 Å, respectively. **e**, **g**, **i** Cross-sections of M2 helices at residues 9′ (top) and -2′ (bottom) for **e** α3β-gly, **g** α3S346Eβ-gly, and **i** α3S346Eβ-gly/2,6-DTBP GlyRs with distances between neighboring Cα shown in Å.

The phosphorylation mimic structure, α3S346Eβ-gly, had a pseudo-5-fold symmetric ECD (Supplementary Fig. 6b, e), but an asymmetric TM conformation, like those observed in other subtypes of heteromeric GlyRs[3,5,47,48] (Fig. 2c, f, g). The 9′ gate remained open, with an asymmetrically constricted -2′ position (2.1 Å radius). Radii along the pore are very similar to those of α3β-gly structure, suggesting a desensitized functional state. Clearly, phosphorylation at S346 (S346E mimetic) changed TM conformation despite it being situated in the long and unstructured M3/M4 loop.

2,6-DTBP induced an asymmetric expanded-open pore conformation in the phosphorylate GlyR structure (S346E mimetic, α3S346Eβ-gly/2,6-DTBP, Fig. 2c, h, i), while maintaining a pseudo-5-fold symmetric ECD (Supplementary Fig. 6d, f). Both the 9′ and the -2′ positions dilated asymmetrically, with a minimum pore radius of ~3.9 Å at the -2′ position, which is too large for the expected open GlyR pore based on electrophysiology measurements[50,52]. The pore geometry is very similar to the previously reported expanded/super open states, with minimal radii larger than expected based on the largest permeable anions[5,49–51]. Although 2,6-DTBP led to dramatic changes in channel conformation, its cryo-EM density cannot be unambiguously identified due to resolution limitation (also see Supplementary Fig. 9a and discussion). In addition, the density for the M3/M4 loop is missing in all the structures.

https://doi.org/10.1038/s41467-025-60516-8

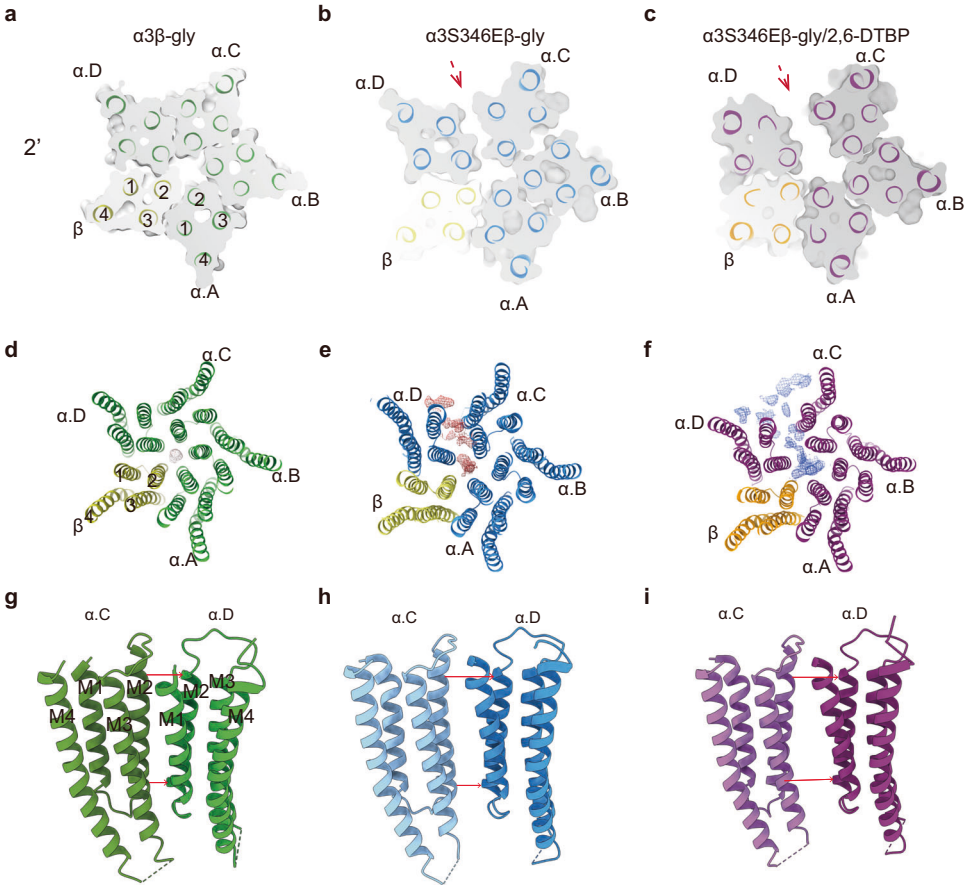

Fig. 3 | Structural changes in the TMD of α3β and α3S346Eβ GlyRs and induced by 2,6-DTBP binding. Z-slice in the TMD at 2′ for **a** α3β-gly, **b** α3S346Eβ-gly, and **c** α3S346Eβ-gly/2,6-DTBP. **d**, **e**, **f** Top-down view of **d** α3β-gly,**e** α3S346Eβ-gly, and **f** α3S346Eβ-gly/2,6-DTBP. Maps are contoured at 5 RMSD. Unmodeled densities are shown as mesh and colored in brown for α3β-gly, red for α3S346Eβ-gly, and blue for α3S346Eβ-gly/2,6-DTBP, respectively. **g, h, i**, Cartoon representation of the TMD interfaces between α.C and α.D subunits for **g** α3β-gly, **h** α3S346Eβ-gly, and **i** α3S346Eβ-gly/2,6-DTBP. The red arrows highlight the distances between adjacent α subunits at -2′ (down) and 19′(top).

Widening of the α3: α3 TM interface underlies pore conformational change

The structures of α3β-gly, α3S346Eβ-gly, and α3S346Eβ-gly/2,6-DTBP are essentially identical in the ECD, showing pseudo-5-fold symmetry in the glycine-bound conformation with capped C-loops (Supplementary Fig. 6g, h). Differences in the ion conduction pore apparently arose from re-arrangements in the TMs.

Changes in distances between neighboring α3 subunit TMs contribute to differences in pore conformations. The TM of α3β-gly GlyR, in the desensitized state, showed 5-fold pseudo-symmetry and tight packing (Fig. 3a, g). Unmodeled densities were only observed in the conduction pore, some of which likely correspond to bound ions (Fig. 3d). In contrast, the distance between two α3 subunits (the one next to the α3: β interface) widened in the phosphorylation mimetic α3S346Eβ-gly structure (Fig. 3b). The same α3: α3 interface widened more dramatically in the α3S346Eβ-gly/2,6-DTBP structure (Fig. 3c). A similar increase in inter-α subunit distance in the TM has been observed before in α1β GlyR and found relevant to channel opening[5]. α3 subunits showed similar positive charges in the TM interface (Supplementary Fig. 5j, k) as α1, likely resulting in electrostatic repulsion and promotion of the widening in interface.

Since only 1 out of 5 TM interfaces significantly widened, 5-fold pseudo-symmetry was broken for both α3S346Eβ-gly and α3S346Eβ-gly/2,6-DTBP GlyR structures. In addition to the ion conduction pores, extra densities were found in the widened inter-α TM gaps (Fig. 3e, f). These densities may represent substances that stabilize the asymmetric TM conformation with larger spaces between adjacent α3: α3 subunits (Fig. 3h, i).

α3 M3/M4 loop approximates the pore upon phosphorylation and 2,6-DTBP binding

The phosphorylation site, S346, is ~50aa away from the ion conduction pore, corresponding to ~140 Å if the loop is fully extended. How phosphorylation at such a distant residue changes pore conformation is intriguing. Unfortunately, the M3/M4 loop density is missing in all cryo-EM structures due to structural flexibility. Single-molecule Förster resonance energy transfer (smFRET) provides a unique solution that allows evaluation of the distance between S346 and the ion conduction pore without the requirement of resolving static structures.

To allow smFRET experiments (Fig. 4a), α3em and βem were engineered to produce $\alpha3_{FRET}\beta_{FRET}$ GlyR, with and without S346E mutation, which accept cysteine-reactive chemical dyes only at α3C358 as the acceptor (LD655), and A1-tag-reactive[53,54] dyes between α3S380 and P381 as the donor (LD555, see methods for details). α3C358 is close to the phosphorylation site S346, and α3S380 is at the intracellular terminus of helix M4, next to the pore. $\alpha3_{FRET}\beta_{FRET}$ GlyR was immobilized on a glass substrate by anchoring the GFP in the β subunit M3/M4 loop, mimicking how GlyRs are anchored at postsynaptic densities[33,34,55]. FRET values in this setting (Fig. 4a) reflect the distance between the phosphorylation site and the ion conduction

https://doi.org/10.1038/s41467-025-60516-8

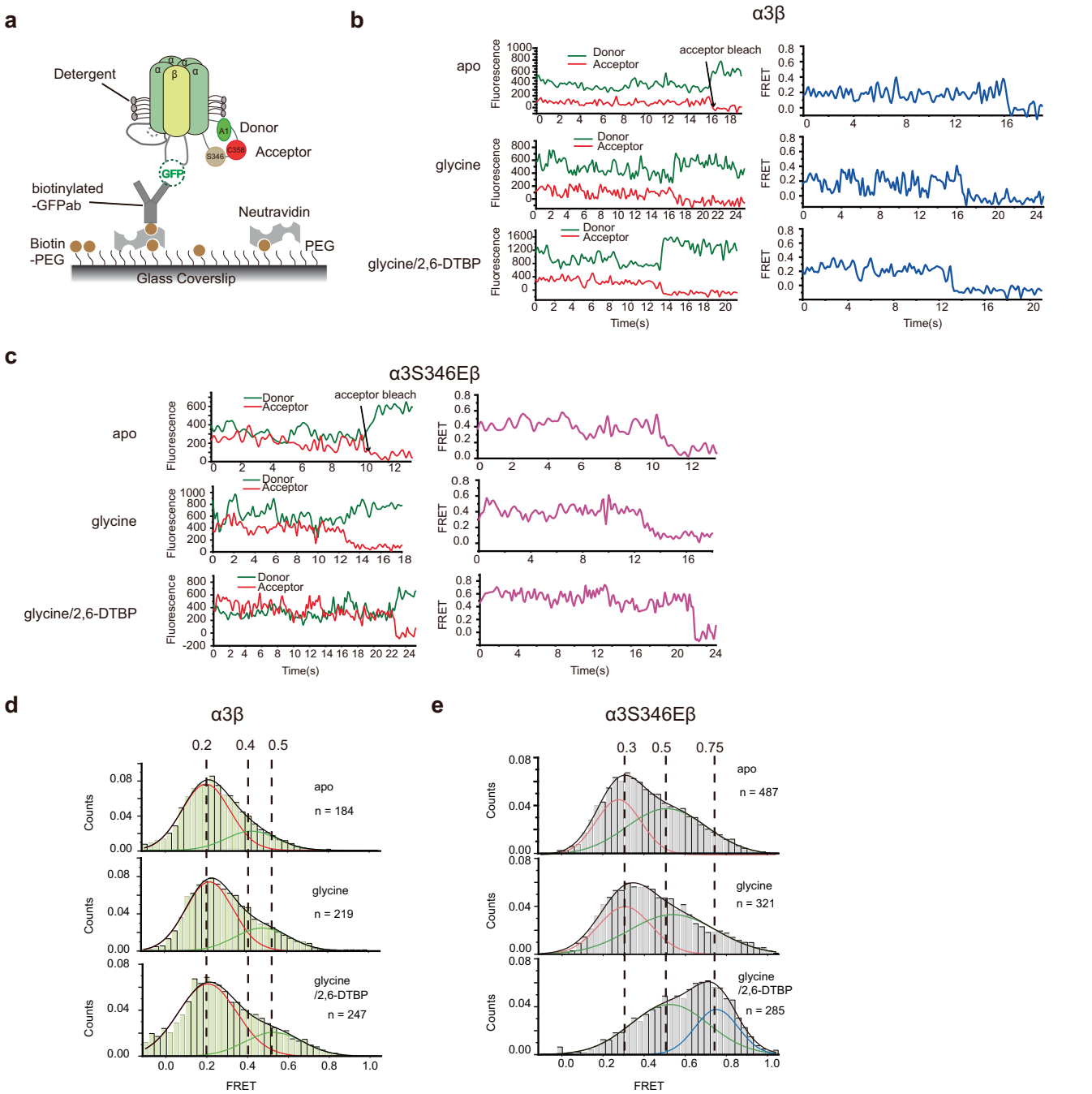

Fig. 4 | α3S346E mutation and 2,6-DTBP modulate conformation of the internal M3/M4 loop in α3S346Eβ GlyR. a Schematic of single-molecule FRET measurements of intra-M3/M4 loop changes. **b**, **c** Representative fluorescence (Left) and FRET (Right) traces of **b** α3β GlyR, and **c** α3S346Eβ GlyR, in apo (top), + glycine (middle) and + glycine + 2,6-DTBP (bottom) conditions. **d**, **e** Histograms of FRET values of **d** α3β and **e** α3S346Eβ GlyRs in the apo (top), + glycine (middle) and +glycine + 2,6-DTBP (bottom) conditions, deconvoluted by fitting with two Gaussians (red and green lines represent each Gaussian and black line shows their sum).

pore. These mutations retained the same glycine-activation (Supplementary Fig. 7a, b) and 2,6-DTBP potentiation (Supplementary Fig. 7c, d) properties as the wild-type α3β GlyR. Our experimental setup had minimal cross-talk/cross excitation based on donor-only and acceptor-only controls (Supplementary Fig. 8f, g).

smFRET measurements suggest structural flexibility in unphosphorylated ($\alpha3_{FRET}\beta_{FRET}$ GlyR) M3/M4 loop, which is marginally affect by glycine activation or 2,6-DTBP binding (Fig. 4b, d). Unlike systems with more defined structural states where well-defined discrete FRET states and transitions were observed[56,57], the FRET signals here appeared more unstable with frequent transitions of non-uniform magnitudes, regardless of whether glycine was present (Fig. 4b, Supplementary Fig. 7e, top and middle panels). Histograms of average FRET values from multiple detections (apo: $n = 184$, with glycine: $n = 219$) shows very similar distributions that decomposes reasonably well into two Gaussians (see methods): one centered around 0.2 FRET value (peak 1) and the other around 0.4 (peak 2), with ~75% of population in peak1. Addition of 2,6-DTBP ($n = 247$) had small effect in shifting peak 2 to ~ 0.5 FRET value, without affecting population distribution (Supplementary Table 2).

Phosphorylation mimetic S346E resulted in higher FRET values, which are further increased after the application of 2,6-DTBP (Fig. 4c, e, Supplementary Fig. 7b). FRET values of $\alpha3_{FRET}$S346Eβ_{FRET} GlyR, both in apo and in the presence of glycine, can be decomposed into two populations: one centered at ~0.3 FRET with 40% counts and another broader peak centered at ~0.5 FRET with ~60% population (Fig. 4e top and middle panels, Supplementary Table 2). These FRET values are significantly larger compared to those without S346E mutation, suggesting a more compact M3/M4 loop conformation that brings the phosphorylation site closer to the ion conduction pore. The addition of 2,6-DTBP dramatically increased FRET, resulting in ~67% population with ~0.5 FRET and ~33% with 0.75 FRET (Fig. 4e bottom panel, Supplementary Table 2), suggesting further compaction of M3/M4 loop towards the pore. That 2,6-DTBP only potentiates phosphorylated α3β GlyR activity (S346E memetic, Fig. 1f, g, i) coincides with the above measurements, where FRET increase is much more evident with the phosphorylation mimic S346E (Fig. 4d, e). 2-state models were chosen since they had lower Bayesian Information Criterion (BIC)[58] scores and likely represent the data better with minimal parameters.

Increased homogeneity in the distances between M3/M4 loops upon phosphorylation and 2,6-DTBP binding

To characterize whether the distance between M3/M4 loops from different α3 subunits is modulated by phosphorylation and 2,6-DTBP binding, we measured FRET efficiencies between C358 of different α3 subunits (Fig. 5a, see methods for details).

Phosphorylation leads to more homogeneous inter-M3/M4 loop distances. Without phosphorylation ($\alpha3_{FRET}\beta_{FRET}$ GlyR), two major populations were found with one peak centered at ~0.25 FRET value (24% counts in apo, $n = 317$; 28% glycine bound, $n = 499$) and the other centered at ~0.45 (76% apo, 72% glycine bound) irrespective of glycine binding (Fig. 5b, d, Supplementary Fig. 8a, c Supplementary Table 3). For the phosphorylation mimetic ($\alpha3_{FRET}$S346Eβ_{FRET} GlyR), a single component was identified centering at ~0.5 FRET, also independent of glycine binding (Fig. 5c, e upper and middle panel, apo $n = 457$, glycine bound $n = 433$, Supplementary Table 3, Supplementary Fig. 8b). Coincidentally, the fluctuation of FRET values with respect to time becomes less prominent (Fig. 5c, Supplementary Fig. 8b, d, e), suggesting a more stable spatial arrangement.

2,6-DTBP showed a phosphorylation-dependent effect on inter-M3/M4 loop distances. Without phosphorylation, 2,6-DTBP shifted FRET distribution from ~25% at ~0.25 FRET and ~75% at ~0.5, to ~68% ~ 0.44 FRET and ~32% at 0.71 (Fig. 5d lower, Supplementary Table 3, n = 417), suggesting increased overall compactness and the emergence of a more compact population. For phosphorylation mimetic mutation, instead of increasing FRET values, 2,6-DTBP binding showed a more subtle effect: it further increased the homogeneity of distance distribution, resulting in a narrower peak in histogram (Fig. 5e lower, $n = 389$). These results clearly show that phosphorylation (mimetic) changes the way that 2,6-DTBP interacts with the M3/M4 loop, coinciding with the fact that only phosphorylated α3β GlyR can be potentiated by 2,6-DTBP.

Potential 2,6-DTBP binding site near α3 M2 and M3 helices

2,6-DTBP binding to α3-containing GlyRs has been reported dependent on residue F388 of the human α3 subunit, near the intracellular opening of the conduction pore[40,46] (Fig. 6a). Considering that propofol and multiple volatile anesthetics bind near M2 and M3 helices in $GABA_A$ receptors[59,60], we suspect that 2,6-DTBP has more extensive interactions with α3β GlyR TM.

A288 is near the extracellular end of M3 helix of GlyR α3 subunit. Its equivalent residue in $GABA_A$ is involved in propofol interaction[59]. Mutating this residue to Ile (α3A288I), which is the equivalent residue of the GlyR β subunit (I312), abolished 2,6-DTBP potentiation for both heteromeric α3β GlyR (Fig. 6d, f) and homomeric α3 GlyR (Supplementary Fig. 9b), similar to the reported α3F388A mutation that is near the intracellular end of M4 helix (Fig. 6e, f and Supplementary Fig. 9b, d). Coincidentally, additional EM densities in the α3S346Eβ-gly/2,6-DTBP structure was observed near α3A288, but not the equivalent position at the β subunit (I312) (Supplementary Fig. 9a). Clearly, 2,6-DTBP binding near α3A288 is essential for its functional effects. We further found that homomeric $\alpha3_{\Delta M3/M4}$ GlyRs, which has the M3/M4 loop removed, can still be robustly potentiated (Supplementary Fig. 9c), underscoring the importance of these likely TM binding sites.

Discussion

Under inflammatory pain conditions, the unstructured M3/M4 loop is phosphorylated (at S346 of the α3 subunit) and causes reduction of α3β GlyR activity. The underlying mechanism was unclear since whether phosphorylation changes α3β GlyR structure was previously unknown, and the flexible M3/M4 loop is absent in all static structures. In this work, we employed smFRET to characterize conformational changes in the flexible M3/M4 loop. Combined with static cryo-EM structures and functional evaluations using electrophysiology and mutagenesis, we show how M3/M4 loop phosphorylation (mimetic) and the binding of an anesthetic derivative 2,6-DTBP regulate α3β GlyR function.

Our findings suggest how S346 phosphorylation in the α3 M3/M4 loop regulates α3β GlyR activity (Fig. 6g, h). It is unlikely through altering the glycine binding pocket[39] since no appreciable difference was identified in structures (Supplementary Fig. 6). Instead, smFRET data showed that phosphorylation led to more compact and stable loop conformation (Figs. 4d, 5d and 6h) and likely resulted in local accumulation of negative charges near ion conduction pore, reducing local Cl^- concentration, consistent with reduction in (unitary) conductance in electrophysiological recordings (Fig. 1d, e, Supplementary Fig. 1g)[42]. Cryo-EM structures further showed a rearranged TM with asymmetric ion conduction pore (Fig. 2f, g and Fig. 3b, e, h). Since phosphorylation (mimetic) is on the M3/M4 loop, TM changes should originate from changes in the M3/M4 loop conformation. Structural changes in the ion conduction pore should also contribute to ion conduction regulation[40,42].

2,6-DTBP interacts with multiple sites in the GlyR TM. A point mutation near the intracellular end of M4 helix, α3F388A, was previously reported to abolished potentiation (Fig. 6e)[41,46]. We further showed that α3A288I mutation (mimicking the I312 residue at the equivalent position in the GlyR β subunit), which is near the extracellular end of M3 helix, also abolished 2,6-DTBP potentiation (Fig. 6d–f, Supplementary Fig. 9b). This site is analogous to a propofol binding site in the $GABA_A$ receptors near M2 and M3 helices[59,60]. Furthermore, four propofol-like EM densities in the α3S346Eβ-gly/2,6-DTBP map was observed near residue α3A288, but not at the equivalent position at the β subunit where the corresponding amino acid residue is I312 (Fig. 6a, b, Supplementary Fig. 9a). Although 2,6-DTBP was not modeled since local resolution was insufficient for unambiguous determination of orientation and interactions, this site is clearly essential for 2,6-DTBP function and is missing in the β subunit.

2,6-DTBP interacts with the M3/M4 loop in a phosphorylation (mimetic)-dependent manner. Without phosphorylation (mimetic), 2,6-DTBP did not change the distance between the M3/M4 and the ion conduction pore (Fig. 4d), but clearly reduced the distances between different M3/M4 loops from adjacent α3 subunits (Fig. 5d). With phosphorylation (mimetic), 2,6-DTBP brought M3/M4 closer to the ion conduction pore (Fig. 4e) but did not reduce (instead only stabilized) M3/M4 loop distances from adjacent α3 subunits (Fig. 5e). Since 2,6-DTBP changed M3/M4 loop conformations regardless of phosphorylation (mimetic), it likely interacts in either cases. However, the modes of interactions should be different, especially

https://doi.org/10.1038/s41467-025-60516-8

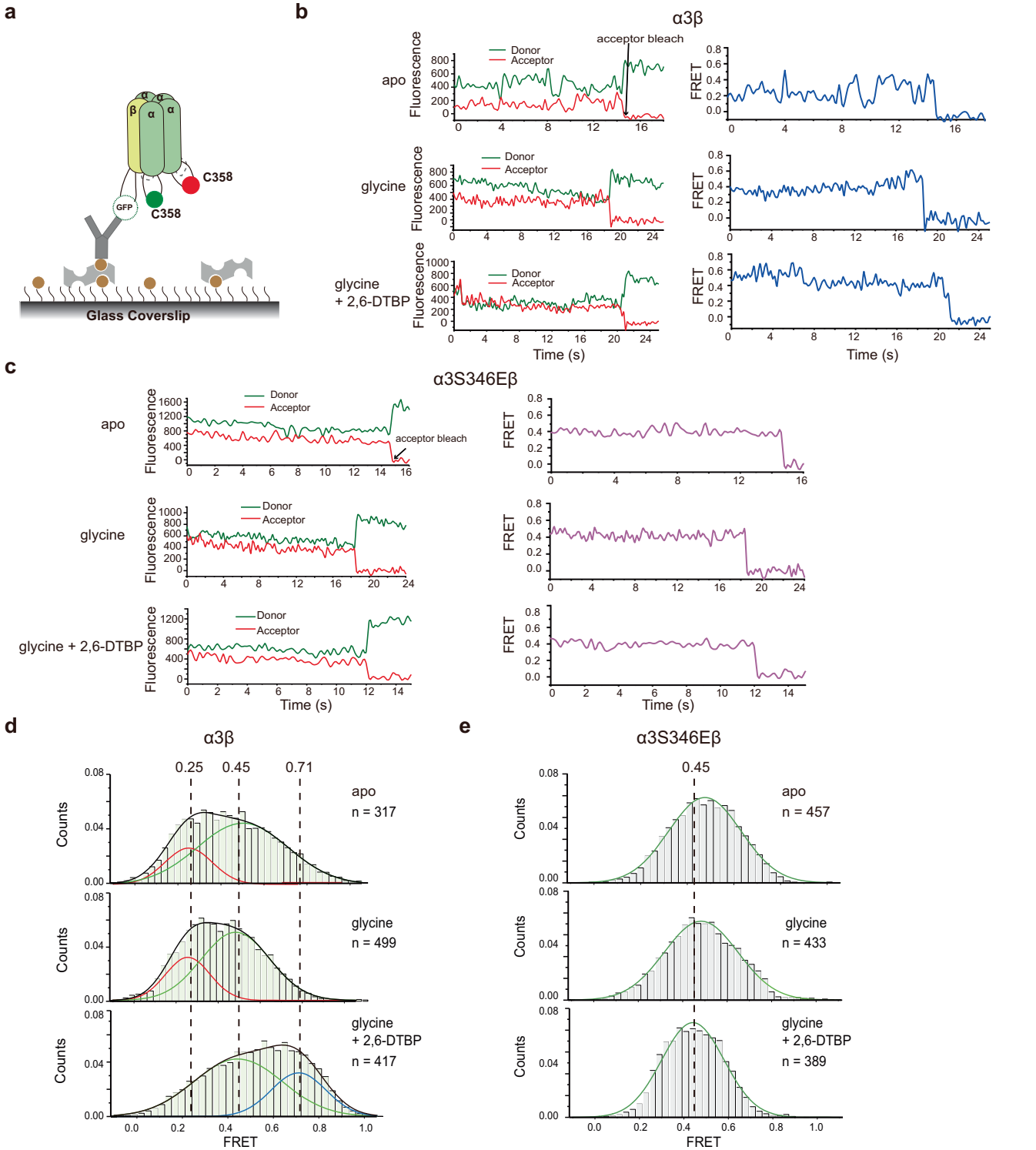

Fig. 5 | α3S346E mutation and 2,6-DTBP affect the distances of M3/M4 loops between different α3 subunits. a Schematic of single-molecule FRET measurements between M3/M4 loops from different α3 subunits. **b**, **c** Representative fluorescence (Left) and FRET (Right) traces of **b** α3β GlyR and **c** α3S346Eβ GlyR in the apo (top), + glycine (middle), and + glycine + 2,6-DTBP (bottom) conditions. **d**, **e** Histograms of FRET values of **d** α3β and **e** α3S346Eβ GlyRs in the apo (top), + glycine (middle), and + glycine + 2,6-DTBP (bottom) conditions. FRET value histograms were deconvoluted by fitting with two Gaussians (red and green lines represent each Gaussian and black lines show their sum). **e** α3S346Eβ GlyRs FRET was fitted with a single Gaussian (green lines).

considering that 2,6-DTBP only brings the phosphorylated (mimetic) M3/M4 loop towards the conduction pore, which explains why 2,6-DTBP only potentiates phosphorylated α3β GlyR (discussed in more detail later).

TM binding is essential for 2,6-DTBP potentiation of both heteromeric α3β GlyR and homomeric α3 GlyR, while M3/M4 loop binding is only required for heteromeric α3β GlyR. We showed that α3A288I and α3F388A mutations abolished potentiation for both heteromeric

https://doi.org/10.1038/s41467-025-60516-8

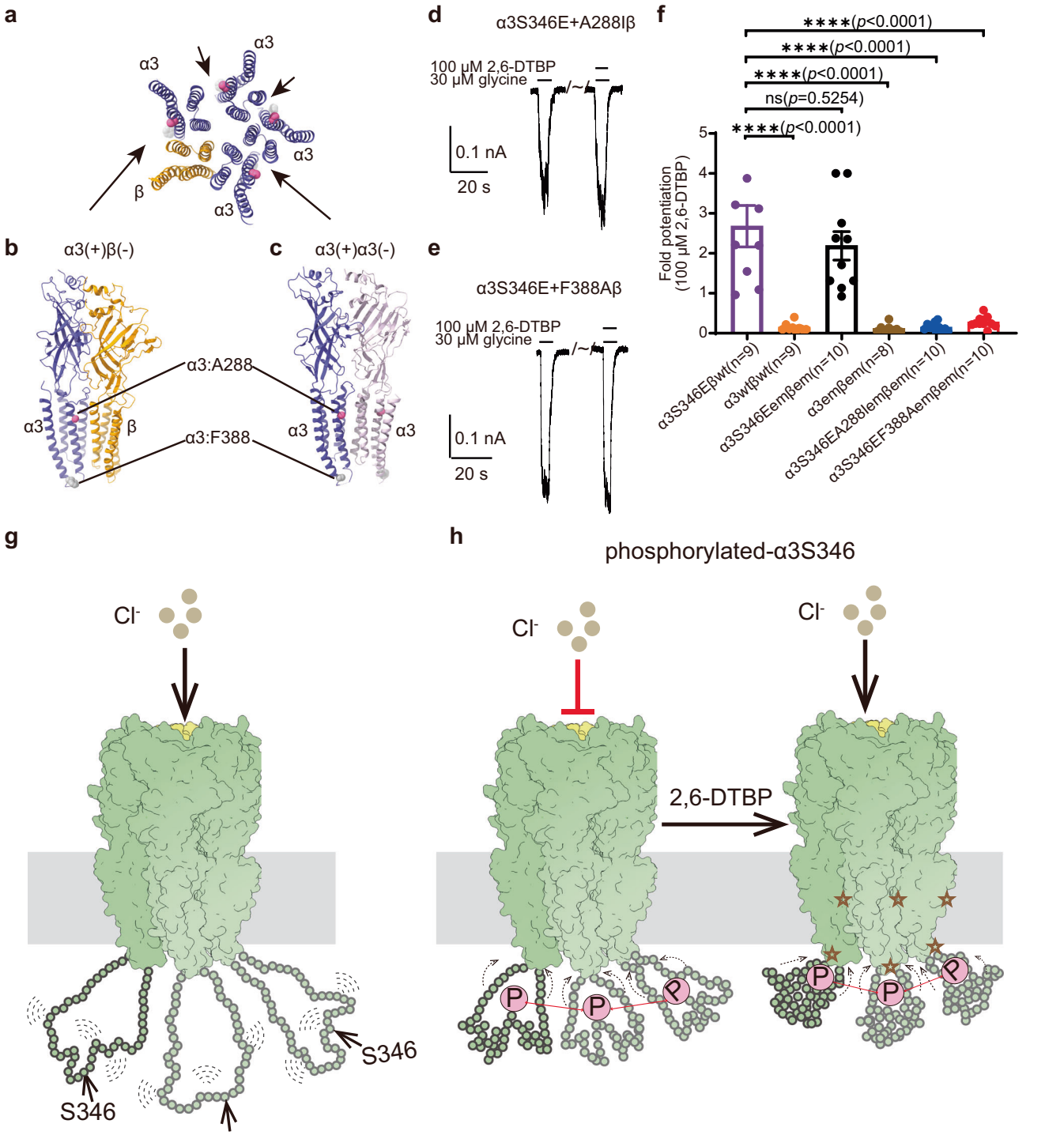

Fig. 6 | Proposed mechanism for α3 M3/M4 loop phosphorylation and 2,6-DTBP modulation of α3β GlyR activity. **a** Top view of TM sectioned near A288, with potential 2,6-DTBP sites indicated by arrows. **b, c** Sideview of **b** α3(+)β(-) and **c** α3(-)β(+) interfaces. A288 and F388 of the α3 subunits are shown as spheres. **d, e** Representative whole-cell recordings of glycine-induced currents from HEK293T cells expressing **d** α3S346EA288Iβ and **e** α3S346EF388Aβ GlyRs with and without 100 μM 2,6-DTBP. **f** Fold-increases of 30 μM glycine-evoked currents by 100 μM 2,6-DTBP. Data are represented as mean ± S.E.M. *P*-values were calculated using one way ANOVA. (**$p < 0.01$; ns, not significant. the exact *p*-values are shown in the figure). **g, h** Mechanistic model of M3/M4 loop and 2,6-DTBP regulation. **g** During the entire functional cycle of non-phosphorylated α3β GlyR (close, open, and desensitized states), the M3/M4 loops of α3 subunits are very flexible and far away from the ion conduction pore in TM. **h** Left: Upon α3S346 phosphorylation, the M3/M4 loop compacts towards the TM, and distances between adjacent M3/M4 loops becomes more stable. These changes result in pore conformational changes and local electronegativity that decrease Cl^- conductance. Right: 2,6-DTBP binds to both TM (stars indicates potential binding sites) and phosphorylated M3/M4 loop, leading to further approximation of loop towards the TM, resulting in pore conformational changes that facilitate Cl^- conduction.

α3β and homomeric α3 GlyRs (see Fig. 6d–f and Supplementary Fig. 9b). To test if interaction with the M3/M4 loop is also strictly required, we removed this loop and expressed homomeric $α3_{ΔM3/M4}$ GlyRs, which 2,6-DTBP can clearly potentiate (Supplementary Fig. 9c).

Our findings seem to converge on resolving a puzzle regarding the peculiar selectivity of 2,6-DTBP potentiation: heteromeric α3β GlyR is potentiated only after phosphorylation, but both phosphorylated and non-phosphorylated homomeric α3 GlyR can be potentiated, although both GlyRs contain the same α3 subunit where the phosphorylation site is located[40,42]. Our data shows that 2,6-DTBP potentiates both phosphorylated and non-phosphorylated homomeric α3 GlyR because binding to the TM alone (near A288 and F388) is sufficient for activation, at saturating 2,6-DTBP concentration we tested. Potentiation of heteromeric α3β GlyR requires phosphorylated M3/M4 loop because binding to the TM alone is not sufficient. M3/M4 loop being brought close to the ion conduction pore is also essential, which only happens after phosphorylation. We note that since only one saturating 2,6-DTBP concentration was tested, it remains possible both M3/M4 loop and TM modulate sensitivity at lower concentrations.

The β subunit underlie the requirement of 2,6-DTBP binding with both TM and phosphorylated M3/M4 loop for α3β GlyR potentiation. This is likely through two mechanisms. First, the β subunit does not allow 2,6-DTBP binding at the M3 helix site (near A288 of α3 but is I312 in β), leading to only four 2,6-DTBP binding sites, as opposed to 5 in homomeric α3 GlyR (Fig. 6a, b and Supplementary Fig. 9a). Fewer 2,6-DTBP bound at the TM may require the proximation and interaction with M3/M4 loop to open GlyR. Second, heteromeric GlyRs open in an asymmetric manner due to opposite charges in the TM of the β subunit compare with the α subunits, as opposed to symmetric dilation of homomeric GlyRs[49,51,61,62]. This involves a widened inter-subunit gap between two adjacent α subunits[5]. Indeed, we observed asymmetric pore expansion in the 2,6-DTBP-bound structure (Fig. 2h, i and Fig. 3c, f, i) and formation of pocket between two α3 subunits (Fig. 3c). Additional unmodeled EM densities were observed in the pocket that likely stabilized the structure. At the same time, smFRET showed that M3/M4 compacted towards the ion conduction pore (Figs. 4e, 6h), where simultaneous binding of 2,6-DTBP to both the TM and the M3/M4 loop may be an underlying mechanism. Compaction of M3/M4 loop, in turn, would promote GlyR open simply due to its conformational change or may through direct interactions at the widened gap and contribute to the unmodeled densities. Since the binding site near α3A288 is very close to the widened gap (Fig. 6b and Supplementary Fig. 9a), it is tempting to speculate that 2,6-DTBP may also interact within the gap and stabilize pore-dilated conformation.

The Cys-loop receptor super family of pentameric ligand gated ion channels (pLGICs) play many critical roles in human physiology throughout the body[63–65], and are highly relevant to sensory function and pharmacological development[26,30,63,64,66–70]. Although the intracellular M3/M4 loops are least conserved, and (mostly) disordered or truncated in available structures of this family of receptors[3,49,71–74], they underly both trafficking and functional regulations. For instances, phosphorylation of the M3/M4 loop (at S380) of the α1 subunit in α1β GlyR has been shown to increase pain through receptor endocytosis[75,76] or reduced function[77]. In addition, post-translational modifications in the M3/M4 loops of $GABA_A$[78,79], nicotinic acetylcholine receptors (nAChRs)[80] and serotonin receptors ($5\text{-}HT_3R$)[81,82] have all been shown to regulation function. The strategy used in this work provides a platform for understanding functional regulation through post-translational modification of the unstructured M3/M4 loop. In addition, 2,6-DTBP interaction with GlyR is reminiscent of propofol and other anesthetics interactions with $GABA_AR$ and homologues, which also involve multiple binding sites including the equivalent site near α3A288 at the extracellular end of M3 helix[59,83–86]. Our findings provide further mechanistic basis for developing pain controlling agents targeting this family of channels.

Due to technical limitations (such as quantity, homogeneity and stability for in-vitro investigation), this work was performed using phosphorylation mimetic mutation, α3S346E, instead of phosphorylated proteins. Although this mimetic recapitulated the functional properties tested here, actual phosphorylated α3β GlyR may differ in multiple ways and thus calls for further investigation. Limited by local resolutions, 2,6-DTBP was not explicitly modeled. Resolution of structures with higher resolutions would be desirable to understand atomic details of 2,6-DTBP interaction. Our smFRET data provided a clear glimpse of how unstructured M3/M4 loop change conformation without the need of static structures. However, due to the flexible nature and lack of discrete conformations, precise distances, and kinetic parameters cannot be reliably derived like in other systems (Supplementary Fig. 7e, f, Supplementary Fig. 8a, b)[56,57,87,88]. In addition, further smFRET experiments in lipid mimetics, such as nanodiscs or lipid vesicles may reveal differences in M3/M4 loop conformation and dynamics. Mutagenesis to bring the M3/M4 loop towards the loop that mimic 2,6-DTBP binding, and/or evaluation of segments of M3/M4 loop function in-trans, may help identify possible interactions, and isolate effects from loop conformational changes.

Methods

Plasmid constructs

The human glycine receptor α3 (NCBI: NP_006520.2), β (NCBI: NP_000815.1) and EP_2(NCBI: NP_000947.2) sequence were amplified from cDNA clones (McDermott Center, UT Southwestern Medical center). The α3em sequence was generated by deletion 9 amnio acids of M3/M4 loop (residues A329-S337). α3S346Eem is the addition of S346E mutation site based on α3em. For the βem construct, we used the previously described βem construct[3,5]. M3/M4 loop (residues N334-N377) was replaced by GGSSAAA-monomeric enhanced green fluorescent protein (EGFP)-SGSGSG. A PA-tag (GVAMPGAEDDVV) and PreScission Protease site (LEVLFQ/GP) were inserted following signal peptide. The α3em and α3wt sequence were subcloned into BacMam expression vector[89]. The β wild type sequence were introduced into pLVX-IRES-ZsGreen1 vector (Clonetech) for electrophysiology. The human prostaglandin E2 receptor EP_2 sequence was inserted into pLVX-IRES-mCherry vector (Clonetech) for electrophysiology. We designed constructs of $α3_{FRET}$, $α3S346E_{FRET}$ and $β_{FRET}$ based on α3em, α3S346Eem, and βem for smFRET imaging, respectively. $α3_{FRET}$ and $α3S346E_{FRET}$ introduced a mutation C41V and inserted an A1 tag (GDSLDMLEWSLM) between α3S380 and α3P381. $β_{FRET}$ introduced a mutation C115S. All mutations were introduced using sites-directed mutagenesis.

Protein expression

Protein α3β and α3S346Eβ was expressed as described before[4,5]. The α3em, α3S346Eem, $α3_{FRET}$, $α3S346E_{FRET}$, βem and $β_{FRET}$ plasmids were transformed into DH10BacY competent cells (Geneva Biotech) to produce bacmids. The bacmids were transfected into Sf9 cells (ATCC, CRL-1711) to generate baculovirus and then recombinant baculovirus titers were measured. Virus was added at MOI (multiplicity of infection) of 2 (at 3βem:1α3em ratio) to HEK293S GnTI$^-$ cells (ATCC, CRL-3022) at a density of 2.5×10^6 cells/ml. 10 mM sodium butyrate was added, and culture temperature was turned to 30 °C after transduction 12 h. Cells were collected after induction 60 h by centrifugation at 30,000 *g* for 20 minutes at 4 °C and stored at −80 °C until further use.

α3β GlyR purification and saposin nanodisc reconstitution for Cryo-EM data collection

Cell pellets were thawed and resuspended in lysis buffer (40 mM Tris pH 8.0, 50 mM NaCl, 2 mM $MgCl_2$, 1 mM $CaCl_2$, 2 mM Glycine, 20 μg/ml Dnase, 2 μg/ml leupeptin, 2 μM pepstatin, 0.8 μM aprotinin, 0.2 mM PMSF) rotated at 4 °C for 30 min under constant stirring, then cell debris was collected by centrifugation at 40,000 *g* for 20 min. The cell

debris was dounced and centrifugated at 40,000 *g* at 4 °C for 20 min. The pellets were further homogenized and solubilized with buffer A (40 mM Tris pH 8.0, 200 mM NaCl, 2 mM $MgCl_2$, 1 mM $CaCl_2$, 2 mM Glycine, 20 µg/ml DNase, 2 µg/ml leupeptin, 2 µM pepstatin, 0.8 µM aprotinin, 0.2 mM PMSF, 0.75% (w/v) DDM, 0.075% (w/v) CHS and 0.075% (w/v) Na Cholate) for 40 min at 4 °C. Supernatant was collected from solubilized membranes by centrifugation at 40,000 g for 30 min, and then PA-tag antibody (NZ-1) resin[90] added to supernatant. The resin was collected and washed with 10 CV buffer B (20 mM Tris pH 8.0, 200 mM NaCl, 2 mM $MgCl_2$, 1 mM $CaCl_2$, 2 mM Glycine, 0.2 mM PMSF, 0.05% (w/v) DDM (Anatrace), 0.005% (w/v) CHS (Anatrace), 0.001% (w/v) Na Cholate (Anatrace)). Then resin bound with protein were mixed with PreScission protease (1:30 v/v) at RT for 1 h to cleave PA tag. The flow through was collected, and resin were washed with another 2 CV buffer B. All proteins were pooled and concentrated to load onto Superose6 increase 10/300 GL column (GE Healthcare) in SEC buffer (20 mM Tris pH8.0, 200 mM NaCl, 2 mM Glycine, 0.05% (w/v) DDM, 0.005% CHS). Reconstitution of α3β GlyR into saposin nanodisc was modified from the published protocol[5]. 1:30:200 molar ratio of α3β: saposin: brain polar lipids extract (BPE) (Avanti) was used. α3β GlyR protein mixed with BPE at room temperature (RT) for 10 min. Saposin protein was added and the mixture was put at RT for another 2 min. The mixture was diluted with buffer (20 mM Tris pH 8.0, 200 mM NaCl, 2 mM Glycine) and incubate on ice for 30 min. Then bio-beads SM-2 (Bio-Rad) were added to the mixture and rotated overnight at 4 °C. After 12 h, old bio-beads were removed and the fresh bio-beads were added for another 10 h. The mixture was centrifuged for 30 min at 4 °C before loading onto Superose 6 increase size exclusion column in SEC buffer (20 mM Tris-HCl pH 8.0, 200 mM NaCl, 2 mM glycine).

Protein (α3β and α3S346Eβ GlyRs) purification in digitonin for Cryo-EM data collection

Cell lysis and protein solubilization by detergent follow the similar protocol as the protein purification for saposin nanodisc reconstitution. Briefly, solubilized membranes were cleared by centrifugation at 40,000 *g* for 30 min. Supernatant was collected and added to PA-tag antibody (NZ-1) resin at RT. The resin was collected and washed with 5 CV buffer B and 5CV buffer C (20 mM Tris pH 8.0, 200 mM NaCl, 2 mM $MgCl_2$, 1 mM $CaCl_2$, 2 mM Glycine, 0.06% (w/v) digitonin (Sigma-Aldrich)). Then, beads were mixed with PreScission protease (1:30 v/v) to cleave PA tag at RT for 1 h. The resin was collected to get flow through, then resin was washed another 2 CV buffer C. Flow through and 2CV washed buffer C were pooled and concentrated to load onto Superose6 increase 10/300 GL column in SEC buffer (20 mM Tris-HCl pH8.0, 200 mM NaCl, 2 mM Glycine, 0.06%(w/v) digitonin). Good peak fractions were collected and concentrated to 6 mg/ml for grids freeze. For the sample with 2,6-DTBP the buffer used throughout the purification process contained 500 µM 2,6-DTBP and another 500 µM 2, 6-DTBP was added to cryo-EM sample for 1 h before grid freezing.

Cryo-EM sample preparation, data collection and image processing

3 mM final concentration (1 × CMC) of Fluorinated fos-choline 8 (Anatrace) was added into cryo-EM sample immediately before freezing. Grids (Quantifoil R1.2/1.3 400-mesh Au holey carbon grid) were glow-discharged. An FEI Vitrobot Mark IV Vitrobot (Thermo Fisher) was used to plunge freeze the grids after application of 3 µl sample at 4°C under 100% humidity.

Micrographs were collected using a Titan Krios microscope (Thermo Fisher) with a K3 Summit direct electron detector (Gatan) operating at 300 kV using the SerialEM data acquisition software. The GIF-Quantum energy filter was set to a slit width of 20 eV. Images were recorded with the pixel size of 0.415 Å in the super-resolution counting mode. Micrographs were dose-fractioned into 50 frames with a dose rate of 1.4 e^-/Å/frame.

2-fold binning (0.83 Å pixel size after binning), motion correction and dose weighting of the movie frames were carried out using the Motioncorr2 program[91]. CTF correction was carried out using the CTFFIND 4 program[92]. The following image processing steps were performed in RELION 4[93]. Particles were initially picked using the Laplacian-of-Gaussian blobs and subjected to 2D classification to obtain good class-averages. Then good 2D classes were used as template for reference-based auto picking. Resulting particles were extracted with 4-fold binning for a further round of 2D classification. Good 2D class-averages were selected and subjected to 3D classification using an initial model downloaded from EMDB database (EMD-23148)[3]. For the α3β-gly GlyR in digitonin sample, 1 out of 6 classes in 3D classification appeared with good density for the entire channel (Supplementary Fig. 2b). A single density blob for GFP was identified for the heteromeric α3β GlyR in digitonin sample. The density arising from GFP fusion on the βem subunit served as fiducial marker to differentiate the β subunit from the structurally similar α subunits. A further 3D classification into 4 classes with non-binned particles (0.83 Å pixel size) without particle alignment was performed. Partial signal subtraction[94] was carried out to focus on the TMD. 1 indistinguishable good class resulted in a final of 19,993 particles. After reverting particles to un-subtracted version, CTF refinement, Bayesian polishing in RELION and non-uniform refinement[95] in cryoSPARC[96], an overall resolution of 3.8 Å was achieved, with local resolutions exceeding 3.5 Å in many regions (Supplementary Fig. 2c–e). For the α3β-gly GlyR in nanodisc sample, 1 out of 3 classes in 3D classification appeared with good density for the entire channel (Supplementary Fig. 2g). A single density blob for GFP was identified for the heteromeric α3β-gly GlyR in nanodisc sample. A further 3D classification into 3 classes with non-binned particles (0.83 Å pixel size) without particle alignment was performed. 1 indistinguishable good class resulted in a final of 40,868 particles. After reverting particles to un-subtracted version, CTF refinement, Bayesian polishing in RELION and non-uniform refinement in cryoSPARC, an overall resolution of 3.8 Å was achieved, with local resolutions exceeding 3.5 Å in many regions (Supplementary Fig. 2h–j). For the α3S346Eβ-gly GlyR in digitonin, 1 out of 4 classes in 3D classification appeared with good density for the entire channel (Supplementary Fig. 3b). A single density blob for GFP was identified for the heteromeric α3S346Eβ-gly GlyR sample. A further 3D classification into 4 classes with non-binned particles (0.83 Å pixel size) without particle alignment was performed. 1 indistinguishable good class resulted in a final of 9,628 particles. After reverting particles to un-subtracted version, CTF refinement, Bayesian polishing in RELION and non-uniform refinement in cryoSPARC, an overall resolution of 3.7 Å was achieved, with local resolutions exceeding 3.0 Å in many regions (Supplementary Fig. 3c–e).

For the α3S346Eβ-gly/2,6-DTBP GlyR in digitonin sample, 1 out of 6 classes in 3D classification appeared with good density for the entire channel (Supplementary Fig. 3g). A single density blob for GFP was identified for the heteromeric GlyR α3S346Eβ-gly/2,6-DTBP GlyR sample. A further 3D classification into 4 classes with non-binned particles (0.83 Å pixel size) without particle alignment was performed. 1 indistinguishable good class resulted in a final of 22,755 particles. After reverting particles to un-subtracted version, CTF refinement, Bayesian polishing in RELION and non-uniform refinement in cryoSPARC, an overall resolution of 3.6 Å was achieved, with local resolutions exceeding 2.5 Å in many regions (Supplementary Fig. 3h–j). Resolutions were estimated by applying a soft mask around the protein densities with the Fourier Shell Correlation (FSC) 0.143 criterion. Local resolutions were calculated using Resmap[97].

Model building and refinement

Models of α3β-gly (in digitonin and nanodisc) and α3S346Eβ-gly GlyRs were built by fitting the structure of heteromeric human α1β desensitized state (PDB ID: 8DN4)[5] into the Cryo-EM density maps of α3β-gly

(in digitonin and nanodisc) and α3S346Eβ-gly GlyRs using Chimera[98] and Coot[99]. Model of α3S346Eβ-gly/2,6-DTBP GlyR was built by fitting the structure of heteromeric human α1β expanded-open state (PDB ID: 8DN2)[5] into the Cryo-EM density map of α3S346Eβ-gly/2,6-DTBP using Chimera[98] and Coot[99]. The atomic model was manually adjusted in Coot. The final models were refined with real-space refinement module and validated with the comprehensive validation module in PHENIX package[100,101]. Fourier shell correlation (FSC) curves were calculated between the refined atomic model and the work/free half maps as well as the full map, to assess the correlation between the model and the density map. Statistics of cryo-EM data processing and model refinement are listed in Supplementary Table 1. Pore radii were calculated using the HOLE program[102]. Figs. were prepared in UCSF Chimera[98], ChimeraX[103], and PyMOL[104].

The final model of α3β-gly in nanodisc contained the α3 and β subunit amino acids except the following: α3 subunit of chain A (total 422aa, 349aa built, 73aa not built) A1-P7, K312-F328, D338-D382 and Q428 - D431; α3 subunit of chain B (total 422aa, 340aa built, 82aa not built) A1-M8, H311-F328, D338-D382 and H423- D431; α3 subunit of chain C (total 422aa, 345aa built, 77aa not built) A1-A6, H311-F327, D338-D382 and H423-D431; α3 subunit of chain D (total 422aa, 342aa built, 25aa not built) A1-M8, H311-F327, D338-M384, H427-D431. β subunit (total 444aa, 348aa built, 74aa not built) K1-R28, GSSAAA-EGFP-SGSGSG insertion and V378-P442.

The final model of α3β-gly in digitonin contained amino acids except the following: α3 subunit of chain A (total 422aa, 345aa built, 77aa not built) A1-M8, E313-F327, D338-R384 and H427-D431; α3 subunit of chain B (total 422aa, 340aa built, 82aa not built) A1-M8, K311-F327, D338-R384 and H423-D431; α3 subunit of chain C (total 422aa, 343aa built,79aa not built) A1-M8, E313-F327, D338-R384 and H423-D431; α3 subunit of chain D (total 422aa, 343aa built, 79aa not built) A1-M8, H311- F327, D338-K386 and H427-D431. The model of β subunit forα3β-gly in digitonin is the same as α3β GlyR-gly in nanodisc.

The final model of α3S346Eβ-gly contained amino acids except the following: α3 subunit of chain A (total 422aa, 343aa built, 79aa not built) A1-P7,H311-F327, D338-R385 and D425-D431; α3 subunit of chain B (total 422aa, 331aa built, 81aa not built) A1-P7, H311- F327, D338-R385 and H423-D431; α3 subunit of chain C (total 422aa, 336aa built, 31aa not built) A1-P7, H311-F327, D338-R385 and H423- D431; α3 subunit of chain D (total 422aa, 342aa built, 80aa not built) A1-P7, H311-F327, D338-R385 and H423- D431. The model of β subunit of α3S346Eβ-gly is the same as α3β GlyR-gly in nanodisc.

The final model of α3S346Eβ-gly/2,6-DTBP contained the α3 and β subunit amino acids except the following: α3 subunit of chain A (total 422aa, 344aa built, 78aa not built) A1-M8, K312-F327, D338- R385 and I426- D431; α3 subunit of chain B (total 422aa, 334aa built, 81aa not built) A1-M8, K312-F327, D338- R385 and H423- D431; α3 subunit of chain C (total 422aa, 341aa built, 83aa not built) A1-P7, H311-F327, D338- R385 and H423- D431; α3 subunit of chain D (total 422aa, 345aa built, 79aa not built) A1-P7, H311-F327, D338-R385 and H427-D431. The model of α3S346Eβ-gly/2,6-DTBP β subunit is the same as α3β GlyR -gly in nanodisc.

Fluorescence-Detection Size-Exclusion Chromatography (FSEC) expression assay

Fluorescence was detected using the RF-20Axs fluorescence detector for HPLC (Shimadzu, Japan) (GFP excitation: 480 nm, emission: 512 nm) as EGFP was fused into βem construct for FSEC assay. 2 μl of Lipofectamine 3000 (Thermo Fisher Scientific, US) mixing with 1 μg of plasmid (at 1α3:3β ratio), was transfected into HEK293T cells for 12 well plates, each well. Cells were incubated in a CO_2 incubator (37 °C, 8% CO_2) for 48 h after transfection and solubilized with 50 μl buffer B for 1 h. After centrifugation (40,000 *g*, 30 min), 50 μl of the sample was applied to a Superose 6 Increase 10/300 GL column (GE Healthcare) equilibrated with buffer D (20 mM Tris pH 8.0, 200 mM NaCl, 2 mM glycine, 0.025%DDM) for the FSEC assay.

Whole cell patch clamp

The glycine EC_{50} values were measured on α3β GlyR and α3S346Eβ GlyR expressed in HEK293T cells (ATCC, CRL-3216). Plasmids were transiently transfected using Lipofectamine 3000 reagent (Invitrogen). Total 0.8 μg of DNA was transfected at 1α3:3β ratios for 35 mm dish. Whole-cell recordings were made after 17-24 h of transfected at 22 °C. GFP fluorescence was used to identify the cells expressing the heteromeric α3β and α3S346Eβ GlyRs. The bath solution contained (in mM): 10 HEPES-NaOH pH 7.4, 10 KCl, 125 NaCl, 2 $MgCl_2$, 1 $CaCl_2$, and 10 glucose. The pipette solution contained (in mM): 10 HEPES-NaOH pH 7.4, 150 KCl, 5 NaCl, 2 $MgCl_2$, 1 $CaCl_2$, and 5 EGTA. The resistance of borosilicate glass pipettes is between 2~7 MΩ. The voltage was held at −70 mV, and a Digidata 1550B digitizer (Molecular Devices) was connected to an Axopatch 200B amplifier (Molecular Devices) for data acquisition. Analog signals were filtered at 1 kHz and subsequently sampled at 20 kHz and stored on a computer running pClamp 10.5 software. Data analysis was performed by Origin 2018 software (Origin Lab). Hill1 equation was used to fit the dose-response data and derive the EC_{50} (*k*) and Hill coefficient (*n*). For glycine dose response experiment, we fit the data using equation $I = I_0 + (I_{\max} - I_0)\frac{x^n}{k^n + x^n}$, where *I* is current, I_O is the basal current (accounting mostly for leak, very close to 0), I_{max} is the maximum current, and *x* is glycine concentration. All start point is fixed at 0 during fit. Measurements were from 7–11 cells, mean and S.E.M. values were calculated for each data point.

For experiments of PGE_2 modulation GlyR, total 1 μg of plasmid (0.6 μg GlyR at 1α3:3β ratios and 0.4 μg EP_2) was transfected for 35 mm dish. Whole-cell recordings were made after 17–24 h of transfected at 22 °C. Both in the presence of GFP (GlyR) and mCherry (EP_2) fluorescence were used to identify the cells co-expressing the heteromeric α3β GlyR and EP_2 receptor. PGE_2 (10 μM concentration used) was applied by perfusion system at a rate of 1–2 ml/min. At least 5 times the current response evoked by 1 mM glycine was recorded before application of PGE_2. After application PGE_2 for about 2 minutes, the currents reached steady state. This steady state of inhibition was maintained for another 3 min with PGE_2 application. Then bath solution without PGE_2 was applied to wash out.

2,6-DTBP (100 μM concentration used) was also applied by the perfusion system at a rate of 1–2 ml/min. After 3 to 5 times the current response evoked by 30 μM glycine of baseline recording, 2,6-DTBP (100 μM) was applied to bath solution for 4–6 min until the currents increase reaching saturation. The increase in current is recorded every 40 seconds.

Protein purification and labeling for smFRET

Cell lysis and protein solubilization by detergent follow the protocol as the protein purification for saposin nanodisc reconstitution except that 20 mM HEPES-NaOH, pH7.4 was used instead of 20 mM Tris-HCl, pH 8.0. Peak fractions of protein were collected and concentrated to 1 mg/ml. $\alpha_{FRET}\beta_{FRET}$ was equally divided into two parts. One part protein was labeled with CoA-LD555 and LD655-MAL. The protocol as described below: 10 μM TCEP was added to the protein, then incubated for 30 min on ice. $\alpha_{FRET}\beta_{FRET}$ was labeled first by incubating the protein with LD655-MAL at 1:3 (protein: LD655-MAL) molar ratio at 4 °C for overnight in the dark. $\alpha_{FRET}\beta_{FRET}$ was labeled further by incubating the protein with 20 μM AcpS, 10 μM CoA-LD555, 20 mM $MgCl_2$, 20 mM HEPES-Na, pH 7.4 at RT for 4 h, protecting from light. Another part of the protein was labeled with LD555-MAL and LD655-MAL in the dark at a 1:3:3 molar ratio (protein: LD555-MAL: LD655-MAL). To remove free dye, the solution with labelled protein was then loaded onto PD-10 desalting column (GE Healthcare) equilibrated in the buffer E (20 mM HEPES-NaOH, pH7.4, 200 mM NaCl, 0.03% (w/v) DDM, 0.003% (w/v)

CHS), and the resulting flow-through was loaded onto a second desalting column equilibrated in buffer E. The flow-through containing pure labeled protein was centrifuged at 18,000 *g* for 1 h at 4 °C to remove insoluble aggregates. FRET-Labeled $\alpha_{FRET}\beta_{FRET}$ were aliquoted and frozen at -80 °C, and freshly thawed before the experiments.

For donor-only and acceptor-only controls, bovine serum albumin (BSA) was dissolved at 2 mg/ml in conjugation buffer (50 mM NaHCO3 pH8, 150 mM NaCl, 1 mM EDTA) and biotinylated using a 3:1 Biotin-(PEG2)-NHS:protein molar ratio at 4 °C overnight. Free biotin was removed using PD-10 columns (GE Healthcare). Biotinylated BSA was subjected to labelling with donor - LD555-melamide or acceptor - LD655-melamide in a 3:1 molar ratio of dye to BSA at 4°C overnight. Free dye was removed using PD-10 columns.

Glass slides preparation for smFRET imaging

The glass slides were prepared based on a published protocol[105]. Briefly, slides were cleaned by soaking for 1.5 h at room temperature in piranha solution (≥98% H_2SO_4 and 30% H_2O_2 in a 3:1 ratio) in jugs. The procedure is carried out in a hood. The glass slides were sonicated for 3 times for 10 s/time (once at the start of soaking, once at 45 min, and once at the end) and then washed with ddH_2O 5 times in a jug. Then the treated glass slides are further soaked in 1 M KOH for another 30 minutes and washed 5 times using running ddH_2O. During soaking with KOH, the glass slides were sonicated for another 3 times for 1 min/time (once at the start of soaking, once at 15 min, and once at the end). After washing procedures, the glass slides are drained on air in a vertical position. The soaked glass slides were covered with 25% mPEG-sliane 5k (Sigma-Aldrich) with 1% Biotin mPEG-silane 5k (Sigma-Aldrich) at 90 °C on a metal plate covered by a Petri dish for 30 min. Finally, the glass slides were washed with running ddH_2O and then drained on air in a vertical position. Coated glass slides were stored at −20 °C until further use.

TIRF-based single-molecule FRET imaging

For direct immobilization of $\alpha_{FRET}\beta_{FRET}$, the imaging surface was first exposed to 0.2 µM NeutrAvidin (Thermo Fisher Scientific) and then 50 nM Biotin Anti-GFP antibody (abcam, ab6658) in buffer F (50 mM HEPES-NaOH, pH7.4, 150 mM NaCl). The surface was washed and exchanged into imaging buffer (50 mM HEPES-NaOH pH 7.4, 150 mM NaCl, 10 mM $MgCl_2$, 0.8% (w/v) glucose). FRET-labeled GlyR variants was diluted to 0.7 nM and bound to a NeutrAvidin/ Biotin anti GFPab-coated glass slide surface for 30 min in imaging buffer with 2 µM 25-nucleotide DNA duplex (IDT) and 10 mg/ml BSA (Jackson Immunoresearch) as surface blocking agents. To measure smFRET in the apo state, imaging was performed in imaging buffer. To measure the effect of glycine on smFRET value, imaging was performed in imaging buffer with 2 2 mM glycine added. To detect the modulation of 2,6-DTBP on M3/M4 loop, imaging was performed in imaging buffer added 2 mM glycine and 500 µM 2,6-DTBP, and waiting for 30 min before imaging recording. For donor/acceptor only controls, respectively labeled BSA was diluted to a final concentration of 1 nM in imaging buffer supplemented with 10 mg/ml unlabeled BSA, and applied to coverslips at room temperature for 30 min. TIRF-based smFRET imaging experiments were performed at 22 °C with a custom-built TIRF microscope. Fluorescence emission from LD555 and LD655 was collected by a 60X, 1.27 NA water immersion objective (Leica), spectrally split in a MultiCam Device (Cairn), and collected with two synchronized Flash 4.0 V3 camera (C13440-20CU, Hamamatsu) with 2 × 2 pixel binning. SmFRET imaging recordings were performed by exciting with the Gem 560 nm laser (Laser Quantum) laser at 50 mW and acquiring 200 frames per movie at a 200 ms/frame rate in both donor and acceptor channels.

Analysis of TIRF-based single-molecule data

Image movies were analyzed with Cornell SPARTAN version 3.7.0[106] following the manual. Molecules were detected as local intensity maxima in the total intensity image that are brighter than a threshold above background levels in an image combining donor and acceptor channels (aligned using the iterative closest points algorithm) averaged over the first 10 frames, and background subtracted with a threshold of 100. The distances of molecules smaller than 3.5 pixels were excluded from analysis. Traces were extracted from the selected intensity maxima by summing the 9 most intense pixels for each fluorescence channel. Selected traces were saved for further analysis if they met the following criteria for experiments recorded with 200 ms (10 ms) time resolution: FRET lifetime > 5, donor acceptor correlation coefficient −1 to 0.5, signal-to-noise >8, #cy3 blinks<4, and remove overlapping traces. Saved races is then manually viewed and selected as all FRET sections for further analysis according following criteria: Donor-acceptor fluorescence exchange time more than 5 s (25 frames); Donor and acceptor fluorescence were found to bleach in a single step. Single-molecule traces showing dynamics before photobleaching. More than 180 molecules at each condition were manually selected, and FRET values for each condition were accumulated in histograms. Histogram distributions were analyzed with a double Gaussian equation to reveal recurring mean FRET values using Origin 2018 software (OriginLab). The correlation results of Gaussian fitting analysis were listed in Supplementary Tables 2 and 3. FRET histograms shown in the results are averaged from the first 25 frames (total 5 s).

Plotting and statistics

Glycine dose-response curves were fitted using Origin 2019pro software (OriginLab). Bar graphs of GlyRs regulation by PGE2 and 2,6-DTBP were plotted using GraphPad Prism (GraphPad Software). Plotting, fitting, and statistical analysis for all single-molecule data were carried out using Origin 2019pro (OriginLab). All errors represent the S.E.M.

Reporting summary

Further information on research design is available in the Nature Portfolio Reporting Summary linked to this article.

Data availability

The density maps for the cryo-em data have been deposited in the Electron Microscopy Data Bank under accession codes EMD-44754 (α3β-gly in nanodisc), EMD-44755 (α3β-gly in digitonin), EMD-44756 (α3S346Eβ-gly in digitonin), EMD-44763 (α3S346Eβ-gly/2,6-DTBP in digitonin). The coordinates have been deposited in the Protein Data Bank under accession codes 9BOY (α3β-gly in nanodisc), 9BOZ (α3β-gly in digitonin), 9BPO (α3S346Eβ-gly in digitonin), 9BP7 (α3S346Eβ-gly/2,6-DTBP in digitonin). The previously published structures 5BKF and 8DN2 used in our data analysis are also available from the PDB. Source data are provided with this paper.

References

1. Lynch, J. W. Molecular structure and function of the glycine receptor chloride channel. *Physiol. Rev.* **84**, 1051–1095 (2004).
2. Lynch, J. W. Native glycine receptor subtypes and their physiological roles. *Neuropharmacology* **56**, 303–309 (2009).
3. Yu, H., Bai, X. C. & Wang, W. Characterization of the subunit composition and structure of adult human glycine receptors. *Neuron* **109**, 2707–2716.e2706 (2021).
4. Zhu, H. & Gouaux, E. Architecture and assembly mechanism of native glycine receptors. *Nature* **599**, 513–517 (2021).
5. Liu, X. & Wang, W. Asymmetric gating of a human heteropentameric glycine receptor. *Nat. Commun.* **14**, 6377 (2023).
6. Kuhse, J. et al. Loss of extrasynaptic inhibitory glycine receptors in the Hippocampus of an AD mouse model is restored by treatment with Artesunate. *Int. J. Mol. Sci.* **24**, 4623 (2023).
7. Armijo-Weingart, L. et al. Loss of glycine receptors in the nucleus accumbens and ethanol reward in an Alzheimer's Disease mouse model. *Prog. Neurobiol.* **237**, 102616 (2024).

8. Piton, A. et al. Systematic resequencing of X-chromosome synaptic genes in autism spectrum disorder and schizophrenia. *Mol. Psychiatry* **16**, 867–880 (2011).
9. Cioffi, C. L. & Guzzo, P. R. Inhibitors of Glycine Transporter-1: Potential therapeutics for the treatment of CNS disorders. *Curr. Top. Med. Chem.* **16**, 3404–3437 (2016).
10. de Bartolomeis, A. et al. Glycine signaling in the framework of Dopamine-Glutamate interaction and postsynaptic density. implications for treatment-resistant schizophrenia. *Front Psychiatry* **11**, 369 (2020).
11. Carvajal-Gonzalez, A. et al. Glycine receptor antibodies in PERM and related syndromes: characteristics, clinical features and outcomes. *Brain* **137**, 2178–2192 (2014).
12. Wu, X., Zhang, H., Shi, M. & Fang, S. Clinical features in antiglycine receptor antibody-related disease: a case report and update literature review. *Front. Immunol.* **15**, 1387591 (2024).
13. Chattipakorn, S. C. & McMahon, L. L. Pharmacological characterization of glycine-gated chloride currents recorded in rat hippocampal slices. *J. Neurophysiol.* **87**, 1515–1525 (2002).
14. Pfeiffer, F. & Betz, H. Solubilization of the glycine receptor from rat spinal cord. *Brain Res.* **226**, 273–279 (1981).
15. Becker, C. M., Hoch, W. & Betz, H. Glycine receptor heterogeneity in rat spinal cord during postnatal development. *EMBO J.* **7**, 3717–3726 (1988).
16. Shiang, R. et al. Mutations in the alpha 1 subunit of the inhibitory glycine receptor cause the dominant neurologic disorder, hyperekplexia. *Nat. Genet.* **5**, 351–358 (1993).
17. Rees, M. I. et al. Hyperekplexia associated with compound heterozygote mutations in the beta-subunit of the human inhibitory glycine receptor (GLRB). *Hum. Mol. Genet.* **11**, 853–860 (2002).
18. Gregory, M. L. et al. A novel GLRA1 mutation associated with an atypical hyperekplexia phenotype. *J. Child Neurol.* **23**, 1433–1438 (2008).
19. Bode, A. et al. New hyperekplexia mutations provide insight into glycine receptor assembly, trafficking, and activation mechanisms. *J. Biol. Chem.* **288**, 33745–33759 (2013).
20. Bode, A. & Lynch, J. W. The impact of human hyperekplexia mutations on glycine receptor structure and function. *Mol. Brain* **7**, 2 (2014).
21. Zeilhofer, H. U., Werynska, K., Gingras, J., Yevenes, G. E. Glycine receptors in spinal nociceptive control-an update. *Biomolecules* **11**, 846 (2021).
22. Chery, N. & de Koninck, Y. Junctional versus extrajunctional glycine and GABA(A) receptor-mediated IPSCs in identified lamina I neurons of the adult rat spinal cord. *J. Neurosci.* **19**, 7342–7355 (1999).
23. Breivik, H., Collett, B., Ventafridda, V., Cohen, R. & Gallacher, D. Survey of chronic pain in Europe: prevalence, impact on daily life, and treatment. *Eur. J. Pain.* **10**, 287–333 (2006).
24. Dubois, M. Y., Gallagher, R. M. & Lippe, P. M. Pain medicine position paper. *Pain. Med* **10**, 972–1000 (2009).
25. Yekkirala, A. S., Roberson, D. P., Bean, B. P. & Woolf, C. J. Breaking barriers to novel analgesic drug development. *Nat. Rev. Drug Discov.* **16**, 545–564 (2017).
26. Harvey, R. J. et al. GlyR alpha3: an essential target for spinal PGE2-mediated inflammatory pain sensitization. *Science* **304**, 884–887 (2004).
27. Zeilhofer, H. U., Wildner, H. & Yevenes, G. E. Fast synaptic inhibition in spinal sensory processing and pain control. *Physiol. Rev.* **92**, 193–235 (2012).
28. Lynch, J. W. & Callister, R. J. Glycine receptors: a new therapeutic target in pain pathways. *Curr. Opin. Investig. Drugs* **7**, 48–53 (2006).
29. Peiser-Oliver, J. M. et al. Glycinergic modulation of pain in behavioral animal models. *Front. Pharm.* **13**, 860903 (2022).
30. San Martin, V. P., Sazo, A., Utreras, E., Moraga-Cid, G. & Yevenes, G. E. Glycine receptor subtypes and their roles in nociception and chronic pain. *Front. Mol. Neurosci.* **15**, 848642 (2022).
31. Song, Y. M. & Huang, L. Y. Modulation of glycine receptor chloride channels by cAMP-dependent protein kinase in spinal trigeminal neurons. *Nature* **348**, 242–245 (1990).
32. Meyer, G., Kirsch, J., Betz, H. & Langosch, D. Identification of a gephyrin binding motif on the glycine receptor beta subunit. *Neuron* **15**, 563–572 (1995).
33. Kirsch, J., Wolters, I., Triller, A. & Betz, H. Gephyrin antisense oligonucleotides prevent glycine receptor clustering in spinal neurons. *Nature* **366**, 745–748 (1993).
34. Kirsch, J., Kuhse, J. & Betz, H. Targeting of glycine receptor subunits to gephyrin-rich domains in transfected human embryonic kidney cells. *Mol. Cell. Neurosci.* **6**, 450–461 (1995).
35. Unterer, B., Becker, C. M. & Villmann, C. The importance of TM3-4 loop subdomains for functional reconstitution of glycine receptors by independent domains. *J. Biol. Chem.* **287**, 39205–39215 (2012).
36. Schaefer, N., Roemer, V., Janzen, D. & Villmann, C. Impaired glycine receptor trafficking in neurological diseases. *Front. Mol. Neurosci.* **11**, 291 (2018).
37. Langlhofer, G. & Villmann, C. The intracellular loop of the glycine receptor: it's not all about the size. *Front. Mol. Neurosci.* **9**, 41 (2016).
38. Xiaofen, L., Weiwei, W. Gating mechanism of the human α1β GlyR by glycine. *bioRxiv*, 2023.2008.2008.552474 (2023).
39. Han, L., Talwar, S., Wang, Q., Shan, Q. & Lynch, J. W. Phosphorylation of alpha3 glycine receptors induces a conformational change in the glycine-binding site. *ACS Chem. Neurosci.* **4**, 1361–1370 (2013).
40. Acuna, M. A. et al. Phosphorylation state-dependent modulation of spinal glycine receptors alleviates inflammatory pain. *J. Clin. Invest.* **126**, 2547–2560 (2016).
41. Werynska, K. et al. A Glra3 phosphodeficient mouse mutant establishes the critical role of protein kinase A-dependent phosphorylation and inhibition of glycine receptors in spinal inflammatory hyperalgesia. *Pain* **162**, 2436–2445 (2021).
42. Moraga-Cid, G. et al. Modulation of glycine receptor single-channel conductance by intracellular phosphorylation. *Sci. Rep.* **10**, 4804 (2020).
43. Hosl, K. et al. Spinal prostaglandin E receptors of the EP2 subtype and the glycine receptor alpha3 subunit, which mediate central inflammatory hyperalgesia, do not contribute to pain after peripheral nerve injury or formalin injection. *Pain* **126**, 46–53 (2006).
44. Krasowski, M. D. et al. General anesthetic potencies of a series of propofol analogs correlate with potency for potentiation of gamma-aminobutyric acid (GABA) current at the GABA(A) receptor but not with lipid solubility. *J. Pharm. Exp. Ther.* **297**, 338–351 (2001).
45. Tibbs, G. R. et al. HCN1 channels as targets for anesthetic and nonanesthetic propofol analogs in the amelioration of mechanical and thermal hyperalgesia in a mouse model of neuropathic pain. *J. Pharm. Exp. Ther.* **345**, 363–373 (2013).
46. Moraga-Cid, G., Yevenes, G. E., Schmalzing, G., Peoples, R. W. & Aguayo, L. G. A Single phenylalanine residue in the main intracellular loop of alpha1 gamma-aminobutyric acid type A and glycine receptors influences their sensitivity to propofol. *Anesthesiology* **115**, 464–473 (2011).
47. Zhu, H., Gouaux, E. Architecture and assembly mechanism of native glycine receptors. *Nature*, **599**, 513–517 (2021).
48. Gibbs, E. et al. Conformational transitions and allosteric modulation in a heteromeric glycine receptor. *Nat. Commun.* **14**, 1363 (2023).
49. Du, J., Lu, W., Wu, S., Cheng, Y. & Gouaux, E. Glycine receptor mechanism elucidated by electron cryo-microscopy. *Nature* **526**, 224–229 (2015).

50. Cerdan, A. H. & Cecchini, M. On the functional annotation of open-channel structures in the glycine receptor. *Structure* **28**, 690–693 e693 (2020).
51. Yu, J. et al. Mechanism of gating and partial agonist action in the glycine receptor. *Cell*, **184**, 957–968.e21 (2021).
52. Rundstrom, N., Schmieden, V., Betz, H., Bormann, J. & Langosch, D. Cyanotriphenylborate: subtype-specific blocker of glycine receptor chloride channels. *Proc. Natl Acad. Sci. USA* **91**, 8950–8954 (1994).
53. Zhou, Z. et al. Genetically encoded short peptide tags for orthogonal protein labeling by Sfp and AcpS phosphopantetheinyl transferases. *ACS Chem. Biol.* **2**, 337–346 (2007).
54. Yin, J., Lin, A. J., Golan, D. E. & Walsh, C. T. Site-specific protein labeling by Sfp phosphopantetheinyl transferase. *Nat. Protoc.* **1**, 280–285 (2006).
55. Kim, E. Y. et al. Deciphering the structural framework of glycine receptor anchoring by gephyrin. *EMBO J.* **25**, 1385–1395 (2006).
56. Asher, W. B. et al. GPCR-mediated beta-arrestin activation deconvoluted with single-molecule precision. *Cell* **185**, 1661–1675 e1616 (2022).
57. Wang, L. et al. Characterization of the kinetic cycle of an ABC transporter by single-molecule and cryo-EM analyses. *eLife* **9**, e56451 (2020).
58. Schwarz, G. Estimating the dimension of a model. *Ann. Stat.* **6**, 461–464 (1978). 464.
59. Mihic, S. J. et al. Sites of alcohol and volatile anaesthetic action on GABA(A) and glycine receptors. *Nature* **389**, 385–389 (1997).
60. Yip, G. M. et al. A propofol binding site on mammalian GABAA receptors identified by photolabeling. *Nat. Chem. Biol.* **9**, 715–720 (2013).
61. Huang, X., Chen, H., Michelsen, K., Schneider, S. & Shaffer, P. L. Crystal structure of human glycine receptor-alpha3 bound to antagonist strychnine. *Nature* **526**, 277–280 (2015).
62. Huang, X., Chen, H. & Shaffer, P. L. Crystal structures of human GlyRalpha3 bound to Ivermectin. *Structure* **25**, 945–950 e942 (2017).
63. Sine, S. M. & Engel, A. G. Recent advances in Cys-loop receptor structure and function. *Nature* **440**, 448–455 (2006).
64. Nemecz, A., Prevost, M. S., Menny, A. & Corringer, P. J. Emerging molecular mechanisms of signal transduction in pentameric ligand-gated ion channels. *Neuron* **90**, 452–470 (2016).
65. Thompson, A. J., Lester, H. A. & Lummis, S. C. The structural basis of function in Cys-loop receptors. *Q Rev. Biophys.* **43**, 449–499 (2010).
66. Knabl, J. et al. Reversal of pathological pain through specific spinal GABAA receptor subtypes. *Nature* **451**, 330–334 (2008).
67. Luo, Y., Kusay, A. S., Jiang, T., Chebib, M. & Balle, T. Delta-containing GABA(A) receptors in pain management: Promising targets for novel analgesics. *Neuropharmacology* **195**, 108675 (2021).
68. Hone, A. J. & McIntosh, J. M. Nicotinic acetylcholine receptors in neuropathic and inflammatory pain. *FEBS Lett.* **592**, 1045–1062 (2018).
69. Zeitz, K. P. et al. The 5-HT3 subtype of serotonin receptor contributes to nociceptive processing via a novel subset of myelinated and unmyelinated nociceptors. *J. Neurosci.***22**, 1010–1019 (2002).
70. Liu, Q. Q. et al. Role of 5-HT receptors in neuropathic pain: potential therapeutic implications. *Pharm. Res.* **159**, 104949 (2020).
71. Polovinkin, L. et al. Conformational transitions of the serotonin 5-HT(3) receptor. *Nature* **563**, 275–279 (2018).
72. Zhu, S. et al. Structure of a human synaptic GABAA receptor. *Nature* **559**, 67–72 (2018).
73. Rahman, M. M. et al. Structural mechanism of muscle nicotinic receptor desensitization and block by curare. *Nat. Struct. Mol. Biol.* **29**, 386–394 (2022).
74. Lopez-Sanchez, U. et al. Structural determinants for activity of the antidepressant vortioxetine at human and rodent 5-HT(3) receptors. *Nat. Struct. Mol. Biol.* **31**, 1232–1242 (2024).
75. Zhang, Z. Y. et al. mGluR5/ERK signaling regulated the phosphorylation and function of glycine receptor alpha1ins subunit in spinal dorsal horn of mice. *PLoS Biol.* **17**, e3000371 (2019).
76. Zhang, Z. Y. et al. Ubiquitination and inhibition of glycine receptor by HUWE1 in spinal cord dorsal horn. *Neuropharmacology* **148**, 358–365 (2019).
77. Takazawa, T. et al. Inhibition Mediated by Glycinergic and GABAergic receptors on excitatory neurons in mouse superficial dorsal horn is location-specific but modified by inflammation. *J. Neurosci.***37**, 2336–2348 (2017).
78. O'Toole, K. K. & Jenkins, A. Discrete M3-M4 intracellular loop subdomains control specific aspects of gamma-aminobutyric acid type A receptor function. *J. Biol. Chem.* **286**, 37990–37999 (2011).
79. Sigel, E. & Steinmann, M. E. Structure, function, and modulation of GABA(A) receptors. *J. Biol. Chem.* **287**, 40224–40231 (2012).
80. Kracun, S., Harkness, P. C., Gibb, A. J. & Millar, N. S. Influence of the M3-M4 intracellular domain upon nicotinic acetylcholine receptor assembly, targeting and function. *Br. J. Pharm.* **153**, 1474–1484 (2008).
81. Thompson, A. J., Sullivan, N. L. & Lummis, S. C. Characterization of 5-HT3 receptor mutations identified in schizophrenic patients. *J. Mol. Neurosci.* **30**, 273–281 (2006).
82. Mocatta, J., Mesoy, S. M., Dougherty, D. A. & Lummis, S. C. R. 5-HT(3) Receptor MX Helix contributes to receptor function. *ACS Chem. Neurosci.* **13**, 2338–2345 (2022).
83. Nury, H. et al. X-ray structures of general anaesthetics bound to a pentameric ligand-gated ion channel. *Nature* **469**, 428–431 (2011).
84. Bali, M. & Akabas, M. H. Defining the propofol binding site location on the GABAA receptor. *Mol. Pharmacol.* **65**, 68–76 (2004).
85. Shin, D. J. et al. Propofol is an allosteric agonist with multiple binding sites on Concatemeric Ternary GABA(A) receptors. *Mol. Pharmacol.* **93**, 178–189 (2018).
86. Chen, Z. W. et al. Three classes of propofol binding sites on GABA(A) receptors. *J. Biol. Chem.* **300**, 107778 (2024).
87. Kalinin, S. et al. A toolkit and benchmark study for FRET-restrained high-precision structural modeling. *Nat. methods* **9**, 1218–1225 (2012).
88. Dimura, M. et al. Quantitative FRET studies and integrative modeling unravel the structure and dynamics of biomolecular systems. *Curr. Opin. Struct. Biol.* **40**, 163–185 (2016).
89. Goehring, A. et al. Screening and large-scale expression of membrane proteins in mammalian cells for structural studies. *Nat. Protoc.* **9**, 2574–2585 (2014).
90. Fujii, Y. et al. PA tag: a versatile protein tagging system using a super high affinity antibody against a dodecapeptide derived from human podoplanin. *Protein Expr. Purif.* **95**, 240–247 (2014).
91. Zheng, S. Q. et al. MotionCor2: anisotropic correction of beam-induced motion for improved cryo-electron microscopy. *Nat. Methods* **14**, 331–332 (2017).
92. Rohou, A. & Grigorieff, N. CTFFIND4: Fast and accurate defocus estimation from electron micrographs. *J. Struct. Biol.* **192**, 216–221 (2015).
93. Scheres, S. H. RELION: implementation of a Bayesian approach to cryo-EM structure determination. *J. Struct. Biol.* **180**, 519–530 (2012).
94. Bai, X. C., Rajendra, E., Yang, G., Shi, Y., Scheres, S. H. Sampling the conformational space of the catalytic subunit of human gamma-secretase. *Elife* **4**, e11182 (2015).

95. Punjani, A., Zhang, H. & Fleet, D. J. Non-uniform refinement: adaptive regularization improves single-particle cryo-EM reconstruction. *Nat. Methods* **17**, 1214–1221 (2020).
96. Punjani, A., Rubinstein, J. L., Fleet, D. J. & Brubaker, M. A. cryoSPARC: algorithms for rapid unsupervised cryo-EM structure determination. *Nat. Methods* **14**, 290–296 (2017).
97. Kucukelbir, A., Sigworth, F. J. & Tagare, H. D. Quantifying the local resolution of cryo-EM density maps. *Nat. Methods* **11**, 63–65 (2014).
98. Pettersen, E. F. et al. UCSF Chimera-a visualization system for exploratory research and analysis. *J. Comput. Chem.* **25**, 1605–1612 (2004).
99. Emsley, P., Lohkamp, B., Scott, W. G. & Cowtan, K. Features and development of Coot. *Acta Crystallogr. D. Biol. Crystallogr.* **66**, 486–501 (2010).
100. Adams, P. D. et al. PHENIX: a comprehensive Python-based system for macromolecular structure solution. *Acta Crystallogr D. Biol. Crystallogr.* **66**, 213–221 (2010).
101. Liebschner, D. et al. Macromolecular structure determination using X-rays, neutrons and electrons: recent developments in Phenix. *Acta Crystallogr. D. Struct. Biol.* **75**, 861–877 (2019).
102. Smart, O. S., Neduvelil, J. G., Wang, X., Wallace, B. A. & Sansom, M. S. HOLE: a program for the analysis of the pore dimensions of ion channel structural models. *J. Mol. Graph.* **14**, 354–360 (1996). 376.
103. Pettersen, E. F. et al. UCSF ChimeraX: Structure visualization for researchers, educators, and developers. *Protein Sci.* **30**, 70–82 (2021).
104. Schrödinger, LLC. The PyMOL molecular graphics system, Version 1.8. 2015. (2018).
105. Gidi, Y., Bayram, S., Ablenas, C. J., Blum, A. S. & Cosa, G. Efficient One-Step PEG-Silane Passivation of Glass Surfaces for Single-Molecule Fluorescence Studies. *ACS Appl Mater Interfaces* **10**, 39505–39511 (2018).
106. Juette, M. F. et al. Single-molecule imaging of non-equilibrium molecular ensembles on the millisecond timescale. *Nat. Methods* **13**, 341–344 (2016).

Acknowledgements

We thank Robbie Boyd for preparing tissue culture, molecular biology, and protein biochemistry tools for this project, and helping to edit the manuscript. We thank Dr. Shaotong Zhu for helpful inputs in biochemistry, and all members of the Wang laboratory for helpful discussions. Cryo-EM data were collected at the University of Texas Southwestern Medical Center Cryo-EM Facility, which is funded by the CPRIT Core Facility Support Award RP170644. This work is supported by NIH grant 1R35GM146860 and the McKnight Scholar Award to W.W.

Author contributions

X.L. performed the experiments and analyzed the data. M.K. performed smFRET control experiments. W.W. collected the cryo-EM data and reconstructed density maps. X.L. and W.W. designed the project and wrote the manuscript.

Competing interests

The authors declare no competing interests.

Additional information

Supplementary information The online version contains supplementary material available at https://doi.org/10.1038/s41467-025-60516-8.

Correspondence and requests for materials should be addressed to Weiwei Wang.

Peer review information *Nature Communications* thanks Karin Aubrey, Nikos Hatzakis, Chia-Hsueh Lee, and the other anonymous reviewer(s) for their contribution to the peer review of this work. A peer review file is available.